

Robust and Secure Blockage-Aware Pinching Antenna-assisted Wireless Communication

Ruotong Zhao, *Student Member, IEEE*, Shaokang Hu, *Member, IEEE*, Deepak Mishra, *Senior Member, IEEE*, and Derrick Wing Kwan Ng, *Fellow, IEEE*

Abstract—In this work, we investigate a blockage-aware pinching antenna (PA) system designed for secure and robust wireless communication. The considered system comprises a base station equipped with multiple waveguides, each hosting multiple PAs, and serves multiple single-antenna legitimate users in the presence of multi-antenna eavesdroppers under imperfect channel state information (CSI). To safeguard confidential transmissions, artificial noise (AN) is deliberately injected to degrade the eavesdropping channels. Recognizing that conventional linear CSI-error bounds become overly conservative for spatially distributed PA architectures, we develop new geometry-aware uncertainty sets that jointly characterize eavesdroppers position and array-orientation errors. Building upon these sets, we formulate a robust joint optimization problem that determines per-waveguide beamforming and AN covariance, individual PA power-ratio allocation, and PA positions to maximize the system sum rate subject to secrecy constraints. The highly non-convex design problem is efficiently addressed via a low computational complexity iterative algorithm that capitalizes on block coordinate descent, penalty-based methods, majorization–minimization, the S-procedure, and Lipschitz-based surrogate functions. Simulation results demonstrate that sum rates for the proposed algorithm outperforms conventional fixed antenna systems by 4.7 dB, offering substantially improved rate and secrecy performance. In particular, (i) adaptive PA positioning preserves LoS to legitimate users while effectively exploiting waveguide geometry to disrupt eavesdropper channels, and (ii) neglecting blockage effects in the PA system significantly impacts the system design, leading to performance degradation and inadequate secrecy guarantees.

Index Terms—Physical layer security, beamforming design, imperfect channel state information, flexible antenna.

I. INTRODUCTION

To satisfy the rapidly escalating data traffic demands anticipated in the upcoming sixth-generation (6G) wireless networks, multiple-input multiple-output (MIMO) technology incorporating flexible antenna architectures has been widely envisioned as a critical enabler for effectively exploiting the additional spatial degrees of freedom (DoF) through dynamically reconfiguring the propagation environment and reshaping wireless channels [2]. Depending on the specific implementations, a flexible antenna can be realized by leveraging mechanical actuators [2] or liquid-metal designs [3], with the latter known as fluid antennas; however, their repositioning range is typically limited to only a few wavelengths, often rendering them insufficient to maintain reliable line-of-sight

(LoS) connectivity [4]. Considering that emerging communication systems are migrating toward higher carrier frequencies, pinching antenna (PA) technology has emerged as a novel and promising flexible antenna solution that operates by utilizing dielectric waveguides in which radiating elements are activated by selectively pinching different dielectric particles to simultaneously regulate both path loss and phase shift [5]. This unique mechanism provides stronger LoS connectivity and lower propagation loss compared with alternative flexible antenna approaches [4]. Additionally, PAs facilitate adaptive antenna configurations by simply activating or deactivating elements along the waveguide via pinching operations, offering high flexibility in both the number and placement of radiating elements. This spatial capability enables precise control over complex communication environments and supports effective transmission in dynamic or obstructed scenarios. Moreover, the physics-based hardware model in [6] has demonstrated that the power of PAs can be actively adapted by adjusting their coupling lengths along the waveguide, reinforcing their practical feasibility for dynamic amplitude and phase control.

Despite these advancements, existing studies on PA-assisted systems predominantly rely on overly optimistic assumptions, especially the persistent assumptions of idealized LoS propagation and perfect channel state information (CSI), e.g., [1], [7]–[9]. Indeed, these assumptions inadequately capture the complexities of practical propagation environments, typically assuming a dominant LoS link between PAs and users without explicitly accounting for inevitable blockage effects. However, realistic urban deployments of PAs are inherently subject to numerous blockages, such as buildings and vegetation, which can severely disrupt LoS connectivity [10], [11]. Although [12] demonstrated that PA-assisted systems can achieve significantly lower outage probabilities of data rates compared to conventional antenna systems under probabilistic LoS assumptions, it did not directly investigate the implications of blockages on resource allocation strategies. Similarly, a recent study in [13] analyzed PA performance under blockage effects, exploiting a waveguide architecture with a simplified PA-selection model and reported performance gains. However, its restricted assumptions, e.g., fixed PA positions, single active PA per waveguide, and serving only one user per waveguide, limit spatial flexibility, prevent coherent multi-waveguide beamforming, and ultimately constrain system performance. Furthermore, since existing simplified LoS channel models deviate significantly from real-world conditions, especially at high frequencies such as the millimeter-wave (mmWave) bands [14], a more realistic, blockage-aware channel model

R. Zhao, S. Hu, D. Mishra, and D. W. K. Ng are with the School of Electrical Engineering and Telecommunications, University of New South Wales, Sydney, NSW 2052, Australia (e-mails: ruotong.zhao@student.unsw.edu.au, {shaokang.hu, d.mishra, w.k.ng}@unsw.edu.au).

This article will be presented in part at the 2025 IEEE Globecom [1].

becomes imperative for better performance characterization and accurate resource allocation. Consequently, a comprehensive and rigorous investigation into blockage-aware resource allocation strategies in PA-assisted systems remains underexplored.

On the other hand, since wireless communication is inherently broadcast in nature, confidential signals remain vulnerable to eavesdropping [15], [16]. In this context, the combined effect of blockage and the PA system's pronounced deployment flexibility creates both additional vulnerabilities and new degrees of freedom in system design for physical layer security (PLS). In fact, rather than viewing blockage solely as an inherent impairment, it can be regarded as a design that acts as a spatial barrier and can be strategically exploited to suppress unauthorized signal reception. This makes a blockage-aware PA system model essential for characterizing both new challenges and design opportunities in PLS. While blockages inherently restrict feasible PA deployment regions and complicate the optimization landscape for maintaining reliable LoS connectivity with legitimate users, they can also be strategically harnessed to obstruct LoS paths toward potential eavesdroppers (EAs) through carefully designed PA positions, thereby effectively reducing information leakage and mitigating multi-user interference. However, previous works generally neglected the presence of EAs within PA-assisted systems, and studies such as [1], [12], may therefore underestimate security risks, especially in scenarios where both EAs and PAs are located in close proximity to legitimate users. Indeed, recent studies have highlighted the capability of PA positioning flexibility to enhance PLS by placing antennas closer to legitimate users while distancing them from potential EAs [17], [18]. Nonetheless, these existing investigations addressing PLS in PA-assisted systems remain generally limited to oversimplified configurations, such as considering a single-antenna eavesdropper, neglecting waveguide propagation loss and eavesdropper data rate leakage tolerance. Additionally, although artificial noise (AN) injection is an effective method for mitigating eavesdropping, it has not yet been incorporated into PA-based PLS frameworks [17]–[19].

Existing studies often over-optimistically assume the availability of perfect CSI, e.g. [1], [5]–[8], which is generally impractical. Although pilot-based estimation and geometric propagation modeling have improved CSI acquisition accuracy in modern networks [20], [21], obtaining reliable CSI remains inherently challenging under blockages, especially with constrained training resources [22], [23]. This challenge is indeed further exacerbated in the presence of passive eavesdroppers, whose CSI is extremely difficult to estimate due to their silent and non-cooperative nature [15], [16], [24]. To date, to the best of our knowledge, the only study that considers imperfect CSI in PA systems is [25], which minimizes the transmit power subject to a data rate outage probability constraint. However, its applicability is limited to a single waveguide with a single PA and does not provide a generalized characterization applicable to multiple PAs or multi-waveguide configurations, making the model unsuitable for distributed PA networks. Moreover, unlike conventional antenna arrays, e.g., [15], [23], [24], PA systems feature multiple PAs that can be flexi-

bly distributed along different spatial positions, resulting in geometry-dependent phase variations across propagation paths that may partially cancel or reinforce each other. Consequently, existing near-field CSI-error bounds [16], [23], which rely on co-located antennas and linear approximations, become overly loose and inapplicable for practical distributed PA architectures. Despite the critical importance of capturing these practical effects, current literature lacks a geometric-aware robust CSI-uncertainty framework tailored to PA systems that jointly accounts for blockage conditions, antenna positional displacement, and orientation uncertainties. This significant gap motivates the development of a new uncertainty model capable of accurately characterizing the CSI mismatch in distributed PA networks. It is also important to note that prior studies have often overlooked the intrinsic characteristics of dielectric waveguides, instead treating the power distribution across multiple PAs as uniform [4], [5], [13].

Although several works have examined the impact of dielectric waveguide propagation [6], [26], some are limited to single-PA-per-waveguide configurations, whereas others employ a propagation model that ignores frequency dependence and characterizes attenuation solely by PA location. Unfortunately, such simplified treatment leads to inaccurate modelling of signal attenuation, thereby hindering the efficiency of resource allocation, particularly at higher carrier frequencies [27]. Additionally, although the authors in [1] highlighted that PA systems are notably suitable for multicasting scenarios, it considered only a specific broadcasting setting and did not account for the complex practical environment involving both PLS threats and blockage effects, which jointly restrict feasible PA placements and significantly increase the complexity of resource allocation.

Motivated by these identified research gaps and associated practical challenges, this paper aims to develop a robust and secure resource allocation framework for a blockage-aware PA-assisted system, where a base station is equipped with multiple waveguides, each carrying multiple PAs, to serve multiple single-antenna users in the presence of passive multi-antenna EAs under imperfect CSI. In this regard, we construct a three-dimensional (3D) blockage-aware channel model that jointly captures waveguide attenuation and free-space propagation, which explicitly characterizes the geometric conditions for LoS availability. We adopt a bounded CSI uncertainty for legitimate users, while deriving a new geometry-aware uncertainty bound for passive EAs that captures position- and orientation-induced errors inherent to distributed near-field deployments. On this basis, we formulate a resource allocation design as an optimization problem that jointly determines the beamforming matrix for both signal and the AN covariance, the PA power-ratio, and the PA positions to maximize the system sum rate subject to secrecy constraints that limit information leakage. The resulting design problem is inherently non-convex, not only because it encounters infinitely many inequalities induced by CSI uncertainty, but also due to strong coupling among signal beamforming, PAs' power-ratio, and its placement variable. More challengingly, the PA positions simultaneously influence three PA-dependent functions in the channel model, namely large-scale path loss,

phase shift, and blockage-induced channel coefficients. This joint dependence indicates that variations in PA placement perturb all three functions, thereby further aggravating the nonconvexity. To address these challenges, we develop a block coordinate descent (BCD)-based algorithm to obtain a high-quality suboptimal solution that converges to a stationary point, which alternately addresses two subproblems: (i) updating the beamforming design and PA power coefficient allocations, (ii) updating the PA positions. Each subproblem is handled via tractable reformulations adopting the S-procedure and majorization–minimization (MM). Specifically, the PA positions jointly impact path loss, blockage-induced channel coefficients, and phase alignment, which are intricately coupled yet operate at different spatial scales: the first two on the order of meters, whereas the third operates over only a few wavelengths. Hence, we adopt a two-stage optimization strategy that first determines a coarse placement based on path loss and blockage geometry, and then refines the positions through phase-shift alignment. Simulation results verify the tightness of the proposed uncertainty bound for distributed multi-PA configurations and demonstrate significant gains in system sum rate over conventional fixed-antenna baselines, especially in a blockage-rich environment. They further demonstrate that ignoring blockage can lead to performance degradation and even infeasible secrecy constraints, whereas adaptive PA position establishes a strong LoS for legitimate users while suppressing LoS to EAs, thereby reducing the required AN power to satisfy secrecy targets.

Notation: Throughout this paper, we adopt boldface capital letters to denote matrices and boldface lowercase letters to denote vectors. \mathbf{A}^\top , \mathbf{A}^H , $\text{Tr}(\mathbf{A})$, $\text{Rank}(\mathbf{A})$, and $[\mathbf{A}]_{i,j}$ represent the transpose, the Hermitian transpose, the trace, the rank, and the (i,j) -entry of matrix \mathbf{A} , respectively. $\mathbf{A} \succ \mathbf{0}$ and $\mathbf{A} \succeq \mathbf{0}$ indicate that \mathbf{A} is a positive definite and positive semi-definite matrix, respectively. The operator $\text{diag}(\mathbf{a})$ represents a diagonal matrix whose main diagonal elements are extracted from vector \mathbf{a} , $\text{blkdiag}(\mathbf{A}_1, \dots, \mathbf{A}_n)$ denotes a block diagonal matrix whose diagonal components are $\mathbf{A}_1, \dots, \mathbf{A}_n$, and $\text{Diag}(\mathbf{A})$ denotes a vector whose elements are extracted from the main diagonal elements of matrix \mathbf{A} . $\mathbf{A} \odot \mathbf{B}$ represent the Hadamard product of two matrices \mathbf{A} and \mathbf{B} . \mathbf{I}_N is the $N \times N$ identity matrix; We adopt $\mathbb{C}^{N \times M}$ and $\mathbb{R}^{N \times M}$ to denote the set of all $N \times M$ matrices with complex and real entries, respectively. \mathbb{H}^N represents the set of all $N \times N$ complex Hermitian matrices. The largest eigenvalue of matrix \mathbf{A} and its associated eigenvector are denoted by $\lambda_{\max}(\mathbf{A})$ and $\boldsymbol{\lambda}_{\max}(\mathbf{A})$, respectively. $|\cdot|$, $(\cdot)^*$, \mathbb{R}^+ , and $\mathbb{E}\{\cdot\}$ denote the absolute value, complex conjugate, set of positive real numbers, and statistical expectation, respectively. Moreover, $\|\cdot\|$, $\|\cdot\|_2$, and $\|\cdot\|_*$ denote the norm, nuclear norm, and spectral norm of a vector, respectively. $\text{vec}(\{\mathbf{a}_1, \dots, \mathbf{a}_n\})$ and $\text{vec}\{a_{n,m}\}_{n,m}$ represent the vectorization of the n vectors and nm scalars, respectively. We utilize $j = \sqrt{-1}$, $\Re(a)$, and $\Im(a)$ to represent the imaginary unit of a complex number, the real and imaginary parts of the complex number a , respectively. The circularly symmetric complex Gaussian (CSCG) distribution is denoted by $\mathcal{CN}(\mu, \sigma^2)$, with mean μ and variance σ^2 , and \sim stands for “distributed as”.

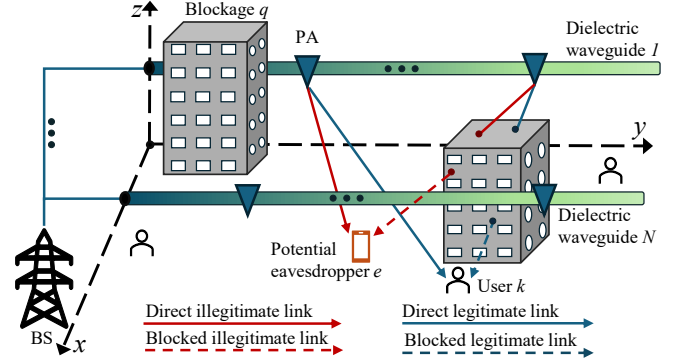


Fig. 1. A downlink PAs-assisted communication system.

II. SYSTEM MODEL

A. Blockage-Aware System Setup

As illustrated in Fig. 1, we consider a blockage-aware downlink PA-assisted communication system subject to potential eavesdropper threats from G non-collaborative ground-based EAs, each attempting to intercept confidential transmissions. Specifically, a base station (BS) feeds signals to N dielectric waveguides, each of length L meters and mounted at a height of d meters above ground level [4]. We assume that each waveguide can accommodate at most M activated PAs¹ and denote the waveguide set as $\mathcal{N} \triangleq \{1, \dots, N\}$. Moreover, each single-antenna user k requires distinct information $s_k \in \mathbb{C}$, satisfying $\mathbb{E}\{|s_k|^2\} = 1$ and $\mathbb{E}\{s_j^* s_k\} = 0, \forall j \neq k$, where $\mathcal{K} = \{1, \dots, K\}$ denotes the set of user indices. Since multiple users are served simultaneously, the transmitted signal $\mathbf{s} \in \mathbb{C}^{N \times 1}$ formed as a superposition of independent signals intended for each user k , along with an AN vector, $\mathbf{v} \in \mathbb{C}^{N \times 1}$, generated by the BS to combat potential EAs, as $\mathbf{s} = \sum_{k=1}^K \mathbf{w}_k s_k + \mathbf{v}$. Note that $\mathbf{w}_k = [w_{k,1}, \dots, w_{k,N}]^\top \in \mathbb{C}^{N \times 1}$ denotes the beamforming vector for user k with elements $w_{k,n} \in \mathbb{C}, \forall n$, indicating the beamforming coefficient on the waveguide n . The AN vector $\mathbf{v} \sim \mathcal{CN}(\mathbf{0}, \mathbf{V})$ is modeled as a complex Gaussian vector with covariance matrix $\mathbf{V} \in \mathbb{H}^N, \mathbf{V} \succeq \mathbf{0}$. Each dielectric waveguide n is subject to a maximum transmit power budget constraint P_n^{\max} , satisfying $\sum_{k=1}^K |w_{k,n}|^2 + \text{Tr}(\mathbf{V}\mathbf{E}_n) \leq P_n^{\max}, \forall n \in \mathcal{N}$, where \mathbf{E}_n is a diagonal selection matrix with $[\mathbf{E}_n]_{n,n} = 1$ and all other entries equal to 0.

To clearly describe the system geometry, a 3D Cartesian coordinate system is employed. Specifically, the feed point of waveguide n is denoted by $\boldsymbol{\psi}_n^{\text{FP}} = [0, y_n^{\text{FP}}, d]^\top$, where y_n^{FP} represents the coordinate along the y -axis corresponding to the feed point of waveguide n . The position of PA m on waveguide n is expressed as $\boldsymbol{\psi}_{n,m}^{\text{Pin}} = [x_{n,m}^{\text{Pin}}, y_n^{\text{FP}}, d]^\top, \forall n \in \mathcal{N}, m \in \mathcal{M} \triangleq \{1, \dots, M\}$, where $x_{n,m}^{\text{Pin}}$ denotes the coordinate along the x -axis for the respective PA. Additionally, we denote user k as u_k , within its 3D position represented as $\boldsymbol{\phi}_k = [x_k, y_k, 0]^\top$, where coordinates x_k and y_k indicate the user's location along the x -axis and y -axis, respectively.

¹One possible practical implementation of a PA system involves mounting PAs on movable platforms along a pre-installed track parallel to the waveguide [4], thereby enabling low-cost deployment and facilitating dense installations with rapid repositioning capability [26].

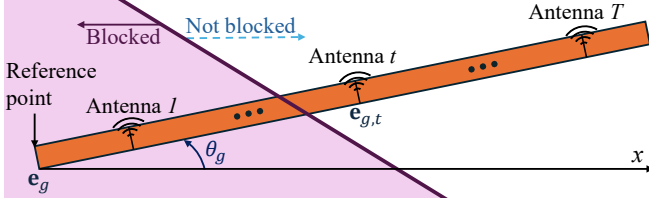


Fig. 2. Illustration of the ULA of EA g , depicting the antenna indexing, blockage regions, and the orientation angle θ_g , with respect to the position x -axis.

Furthermore, there are G non-cooperative potential EAs, indexed by the set $\mathcal{G} \triangleq \{1, \dots, G\}$. In practice, each EA is equipped with a uniform linear array (ULA) comprising $T > 1$ antenna elements, enhancing their capability to intercept the confidential transmissions intended for legitimate users subject to $K + GT \leq N$. Without loss of generality, we assume that the reference point of EA g is located at one end of its ULA [7], denoted as $\mathbf{e}_g = [x_g^E, y_g^E, 0]^T$, with orientation angle θ_g measured relative to the positive x -axis, as shown in Fig. 2. Specifically, antenna t of EA g is the t -th antenna, counting from the reference point, with its position denoted as $\mathbf{e}_{g,t} = [x_{g,t}^E, y_{g,t}^E, 0]^T$, $\forall t \in \{1, \dots, T\}$. The spacing between the reference point and antenna 1, as well as between any two adjacent antennas² of EA g , is set to $\frac{\lambda}{2}$ [7], [16], where $\lambda = \frac{c}{f_c}$ represents wavelength.

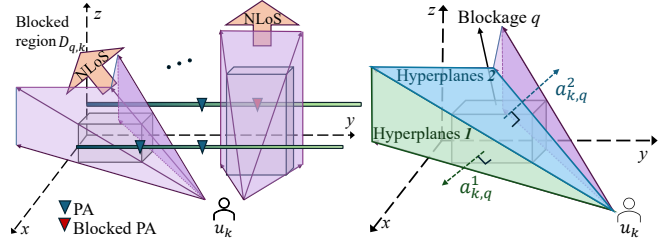
As illustrated in Fig. 3(a), there are Q cube-shaped³ blockages randomly positioned within the service area. Existing works on PA-assisted systems frequently adopt an overly optimistic assumption of ideal LoS propagation conditions, motivated by the inherently long-range and adjustable positioning capabilities of PAs [6], [30], [31]. However, practical deployment scenarios, particularly in urban areas, are characterized by numerous physical obstructions such as buildings and vegetation. Additionally, as frequencies increase and wavelengths decrease, communication links become more susceptible to blockage [26]. Therefore, explicitly incorporating the impact of blockage into system modeling is crucial for improving accuracy and realism. Furthermore, accurately modeling blockage effects also plays a pivotal role in enhancing the effectiveness and precision of subsequent resource allocation and beamforming strategies.

These blockages obstruct the LoS links between a specific user u_k and certain potential PAs located in the corresponding regions, thereby resulting in user-specific blocked areas. We assume that the 3D coordinates and dimensions of all blockages are known a priori⁴ [11]. Specifically, the blocked region attributable to blockage q , $\forall q \in \mathcal{Q} \triangleq \{1, \dots, Q\}$, with respect

²Antenna arrays typically maintain a half-wavelength spacing because this configuration strikes an effective balance between avoiding grating lobes in unintended directions and reducing mutual coupling between antenna elements. It also simplifies the antenna array design by yielding more predictable and easily controlled radiation patterns [28], [29].

³Note that a cubic envelope can be adopted to approximate blockages of arbitrary shapes and is commonly adopted in the literature, e.g., [11], [14].

⁴A practical approach for acquiring building-related information is to utilize an open-source geographic database that provides building contours and height profiles, such as OpenStreetMap [11], [14].



(a) Blockages areas affecting user u_k . (b) Detailed view of blockage q .

Fig. 3. Geometric illustration of a 3D blockage scenario.

to user u_k , can be mathematically represented as [14]:

$$\mathcal{D}_{k,q} = \{\mathbf{x} \in \mathbb{R}^3 \mid (\mathbf{a}_{k,q}^i)^\top \mathbf{x} - b_{k,q}^i \leq 0, i \in \mathcal{I}_{k,q}\}, \forall k, q, \quad (1)$$

where \mathbf{x} represents all possible locations of PAs and $\mathcal{I}_{k,q}$ denotes the set of indices corresponding to the hyperplanes delineating the blocked region $\mathcal{D}_{k,q}$. Here, $(\mathbf{a}_{k,q}^i)^\top$ represents the outward normal vector of hyperplane i , as shown in Fig. 3(b), and $b_{k,q}^i = (\mathbf{a}_{k,q}^i)^\top \phi_k$ is the associated offset determined by the relative geometric positions between u_k and blockage q .

To quantify LoS availability, we define a metric for the placement of PA m on waveguide n , $d_{k,q}^{n,m} = \max_{i \in \mathcal{I}_{k,q}} \{(\mathbf{a}_{k,q}^i)^\top \psi_{n,m}^{\text{Pin}} - b_{k,q}^i\}$. A strictly positive minimum value, i.e., $\min_{q \in \mathcal{Q}} \{d_{k,q}^{n,m}\} > 0$, indicates that the location of this particular PA, $\psi_{n,m}^{\text{Pin}}$, is unblocked by all Q blockages defined with respect to user u_k . In contrast, a non-positive minimum value, i.e., $\min_{q \in \mathcal{Q}} \{d_{k,q}^{n,m}\} \leq 0$, represent that this specific PA is blocked by at least one blockage from the perspective of user u_k . To maximize system performance, PA placements should ideally maintain LoS conditions with legitimate users while opportunistically exploiting blocked conditions with respect to EAs. Note that the evaluation of LoS/blockage conditions for EAs follows the same methodology and procedures outlined above for legitimate users and is omitted for brevity.

B. Channel Model

Considering the impact of blockages, the wireless channel between the M PAs positioned on waveguide n and user u_k can be mathematically modeled by exploiting the LoS⁵ spherical wave near-field channel model [35], [36], denoted as $\mathbf{h}_{n,u_k} = [\tilde{h}_{n,u_k}^1, \dots, \tilde{h}_{n,u_k}^M]^\top \in \mathbb{C}^{M \times 1}$, where $\tilde{h}_{n,u_k}^m = \frac{(\eta_k^{n,m})^{1/2} e^{-j \frac{2\pi}{\lambda} \|\phi_k - \psi_{n,m}^{\text{Pin}}\|}}{\|\phi_k - \psi_{n,m}^{\text{Pin}}\|}$, c , f_c , and λ denote the speed of light, signal carrier frequency, and wavelength in free space, respectively, with

$$\eta_k^{n,m} = \begin{cases} \frac{c^2}{16\pi^2 f_c^2}, & \min_{q \in \mathcal{Q}} \{d_{k,q}^{n,m}\} > 0, \\ 0, & \min_{q \in \mathcal{Q}} \{d_{k,q}^{n,m}\} \leq 0. \end{cases} \quad (2)$$

⁵In near-field configurations, NLoS components typically experience more than 20 dB of additional path loss relative to the LoS path [32], [33]. Indeed, any residual NLoS contribution can be modeled as a norm-bounded perturbation and absorbed into the imperfect CSI uncertainty set [16], [34], without affecting algorithmic structure. We therefore omit explicit NLoS terms.

Thus, a non-zero path gain is assigned only when PA m on waveguide n maintains an unobstructed LoS path to user u_k ; otherwise, the OA contributes no useful signal power to that user. Note that $\mathbf{x}_n^{\text{Pin}} \triangleq \{x_{n,1}^{\text{Pin}}, \dots, x_{n,M}^{\text{Pin}}\}$ is defined as the set of all PA locations associated with waveguide n .

Since the channel coefficient described in (2) is a discontinuous step function, we approximate it with a continuous and differentiable function as in [11], which facilitates subsequent optimization:

$$\eta_k^{n,m} = \hat{\eta} \zeta_k^{n,m}, \quad \hat{\eta} = \frac{c^2}{16\pi^2 f_c^2}, \quad \forall n, m, k, \quad (3)$$

where $\zeta_k^{n,m}$ employs a sigmoid function given by:

$$\zeta_k^{n,m} = \frac{1}{1 + \exp\left(-\vartheta \frac{\min_{q \in \mathcal{Q}} \{d_{k,q}^{n,m}\}}{\|\phi_k - \psi_{n,m}^{\text{Pin}}\|}\right)}, \quad (4)$$

and ϑ is a smoothing parameter that governs the transition rate from LoS to NLoS conditions in (4). The normalization by $\|\phi_k - \psi_{n,m}^{\text{Pin}}\|$ ensures consistent channel blockage evaluation along the same direction with respect to ser u_k [11]. Furthermore, to extend the model to more practical conditions, we consider partial shadowing, where only a subset of antenna elements may be blocked by obstacles, as depicted in Fig. 2, while the remaining elements retain LoS links to the PAs. Similarly, the wireless channel between the M PAs on waveguide n and antenna t of EA g , denoted by $\tilde{\mathbf{h}}_{n,g,t}^{\text{E}} \in \mathbb{C}^{M \times 1}$ follows the same mathematical structure as that for a legitimate user and is therefore omitted for brevity. The blockage-related metric is defined as $d_{g,t,q}^{n,m} = \max_{i \in \mathcal{I}_{g,t,q}} \{(\mathbf{a}_{g,t,q}^i)^\top \psi_{n,m}^{\text{Pin}} - b_{g,t,q}^i\}$, in which $(\mathbf{a}_{g,t,q}^i)^\top$ and $b_{g,t,q}^i$ follow the same geometric definitions and structure as those counterparts introduced for legitimate users.

Since there are M PAs positioned along the same waveguide, the signals transmitted by different PAs differ primarily in their relative phase shifts [4]. Accordingly, the phase-shift vector associated with the M PAs positioned on waveguide n , $\forall n$, excluding propagation losses, is defined as [8]:

$$\tilde{\mathbf{h}}_n(\mathbf{x}_n^{\text{Pin}}) = \left[e^{-j \frac{2\pi \|\psi_{n,1}^{\text{FP}} - \psi_{n,1}^{\text{Pin}}\|}{\lambda}}, \dots, e^{-j \frac{2\pi \|\psi_{n,M}^{\text{FP}} - \psi_{n,M}^{\text{Pin}}\|}{\lambda}} \right]^\top, \quad (5)$$

where the guided wavelength is $\hat{\lambda} = \frac{\lambda}{\eta_{\text{eff}}}$ with $\eta_{\text{eff}} > 1$ represents the effective refractive index of the dielectric waveguide [4], [30]. Therefore, we define the combined phase-shift vector, and the wireless channel vectors of user u_k and antenna t of EA g as $\tilde{\mathbf{h}} = [\tilde{\mathbf{h}}_1^\top, \dots, \tilde{\mathbf{h}}_N^\top]^\top \in \mathbb{C}^{MN \times 1}$, $\tilde{\mathbf{h}}_k = [\tilde{\mathbf{h}}_{1,u_k}^\top, \dots, \tilde{\mathbf{h}}_{N,u_k}^\top]^\top \in \mathbb{C}^{MN \times 1}$, and $\tilde{\mathbf{h}}_{g,t}^{\text{E}} = [(\tilde{\mathbf{h}}_{1,g,t}^{\text{E}})^\top, \dots, (\tilde{\mathbf{h}}_{N,g,t}^{\text{E}})^\top]^\top \in \mathbb{C}^{MN \times 1}$ respectively. Consequently, the effective wireless channel vector towards legitimate user u_k , incorporating both phase-shift and wireless propagation components, is expressed as: $\mathbf{h}_k = \tilde{\mathbf{h}}_k \odot \tilde{\mathbf{h}}, \forall k$. Similarly, the wireless channel matrix toward eavesdropper g , which comprises T antennas, is defined as $\tilde{\mathbf{H}}_{E_g} = [\tilde{\mathbf{h}}_{g,1}^{\text{E}}, \dots, \tilde{\mathbf{h}}_{g,T}^{\text{E}}] \in \mathbb{C}^{MN \times T}$, where the effective channel matrix corresponding to EA g with the phase matrix $\tilde{\mathbf{H}} =$

$\tilde{\mathbf{h}}[1, \dots, 1]^\top \in \mathbb{C}^{MN \times T}$ is $\mathbf{H}_{E_g} = \tilde{\mathbf{H}}_{E_g} \odot \tilde{\mathbf{H}}, \forall g$.

C. PA System CSI Uncertainty Models

In the proposed blockage-aware PA-assisted system, limited pilot resources and the degraded channel estimation accuracy inherent to blocked channels render perfect CSI unattainable, even for legitimate users [21]. Consequently, despite utilizing pilot-based channel estimation techniques, the obtained CSI is inevitably imperfect. Furthermore, acquiring accurate CSI acquisition for EAs is even more challenging. In particular, EAs typically remain silent to conceal their existence and do not proactively cooperate or interact with the BS [16], [24], making precise CSI acquisition for such nodes practically infeasible. To explicitly characterize these uncertainties, we assume that legitimate users leverage the pilot-based channel estimation method [21] and adopt a deterministic CSI uncertainty model [33]. Therefore, the CSI uncertainty range from the MN pinching antennas PAs to legitimate user u_k is defined as:

$$\Psi_k = \{\mathbf{h}_k | \hat{\mathbf{h}}_k + \Delta \mathbf{h}_k, \|\Delta \mathbf{h}_k\|_2 \leq \wp_k, \forall k\}, \quad (6)$$

where $\hat{\mathbf{h}}_k \in \mathbb{C}^{MN \times 1}$ and $\Delta \mathbf{h}_k$ denote the estimated CSI vector and the associated CSI estimation error for legitimate user u_k , respectively. The continuous uncertainty region, Ψ_k , encapsulates all possible realizations of the true channel for the user u_k , where the error norms are bounded by the known parameter $\wp_k > 0$.

On the other hand, although advanced localization techniques, such as various sensing technologies, can yield coarse estimates of an EA's position and orientation [23], passive EAs may still reveal partial CSI information through local-oscillator power leakage at their front ends, even without interacting with the BS [15], [24]. However, unlike in the far field, where a planar wavefront illuminates every element with practically identical amplitude, allowing orientation variations of a ULA can be absorbed into small perturbations of the effective direction of arrival. By contrast, since the impinging wavefront is spherical in the radiative near field, the element-dependent amplitudes and nonlinear phase curvature are highly sensitive to array orientation, thereby elevating orientation to a critical channel parameter for precise focal beamforming [23], [37]. Hence, this work explicitly captures the impacts of imperfect CSI arising from uncertainties in both positions and orientations of EAs. Specifically, we assume that the BS possesses only coarse location information of each EA, denoted as $\{\hat{\mathbf{e}}_g | \hat{\mathbf{e}}_g = [\hat{x}_g^{\text{E}}, \hat{y}_g^{\text{E}}, 0]^\top, \forall g \in \mathcal{G}\}$. Given that the antenna spacing of each EA's ULA is $\frac{\lambda}{2}$ [29], we can further estimate the positions of individual antenna elements as $\hat{\mathbf{e}}_{g,t} = \hat{\mathbf{e}}_g + t \frac{\lambda}{2} \mathbf{u}_g, \forall g, t$, where $\mathbf{u}_g = \mathbf{R}_g(\Delta\theta_g) \hat{\mathbf{u}}_g$, $\mathbf{R}_g(\Delta\theta_g)$ and $\hat{\mathbf{u}}_g$ are the rotation matrix and nominal direction vector for EA g , respectively:

$$\mathbf{R}_g(\Delta\theta_g) \hat{\mathbf{u}}_g = \begin{bmatrix} \cos(\hat{\theta}_g + \Delta\theta_g) \\ \sin(\hat{\theta}_g + \Delta\theta_g) \\ 0 \end{bmatrix}, \quad \forall g. \quad (7)$$

Note that θ_g and $\Delta\theta_g$ are the estimated rotation angle and the corresponding error for EA g from the “+ x ”-axis. Therefore,

the actual position of antenna t at EA g , denoted as $\mathbf{e}_{g,t}$, can be modeled as the sum of the estimated reference location $\hat{\mathbf{e}}_{g,t}$, a common location perturbation⁶, the orientation induced effect $\Delta\mathbf{e}_g$ and $t\frac{\lambda}{2}\mathbf{u}_g$, i.e.,

$$\mathbf{e}_{g,t} = \hat{\mathbf{e}}_g + \Delta\mathbf{e}_g + t\frac{\lambda}{2}\mathbf{u}_g, \|\Delta\mathbf{e}_g\| \leq \varphi_g^E, |\Delta\theta_g| \leq \varphi_g^{\text{arc}}, \forall g, t, \quad (8)$$

where the known bounds $\varphi_g^{\text{arc}}, \varphi_g^E > 0$ reflect the achievable localization and orientation accuracies [16], [23], [39], [40].

Considering the above location-induced uncertainties, the resultant CSI error matrix for EA g , aggregated across all MN PAs, $\Delta\mathbf{H}_{E_g} = \mathbf{H}_{E_g} - \hat{\mathbf{H}}_{E_g} \forall g$, is given by:

$$\Delta\mathbf{H}_{E_g} = \tilde{\mathbf{H}}_{E_g}(\mathbf{E}) \odot \bar{\mathbf{H}} - \tilde{\mathbf{H}}_{E_g}(\hat{\mathbf{E}}) \odot \bar{\mathbf{H}}, \quad (9)$$

where $\hat{\mathbf{H}}_{E_g}$ represents the estimated effective channel matrix constructed from the estimated positions of G EAs, each with T antennas and accounting for orientation uncertainties, denoted collectively as $\hat{\mathbf{E}}$. Meanwhile, \mathbf{E} represents the collections of the actual antenna positions of all EAs. Consequently, the CSI uncertainty region for EA g is expressed as:

$$\Psi_g^E = \{\mathbf{H}_{E_g} | \hat{\mathbf{H}}_{E_g} + \Delta\mathbf{H}_{E_g}, \|\Delta\mathbf{e}_g\| \leq \varphi_g^E, |\Delta\theta_g| \leq \varphi_g^{\text{arc}}, \forall g\}. \quad (10)$$

It is important to emphasize that the coupled CSI uncertainties originate from positioning inaccuracies of EAs in both location and orientation. These uncertainties influence not only the large-scale path-loss terms but also the element-wise phase alignment across the ULA, particularly in near-field propagation. Moreover, the distributed architecture of PA arrays introduces path-specific channel perturbations that may partially offset one another under EA position perturbations, rendering existing linear uncertainty bounds [16] inaccurate to PA systems. Consequently, deriving a tractable yet appropriately geometry-aware uncertainty bound for EA CSI constitutes one of the key technical challenges addressed in this work and is detailed in Section III.B.

D. Waveguide Propagation Model

Existing studies often oversimplify PA systems, limiting the accuracy and effectiveness of resource allocation strategies. To overcome this limitation, this work adopts a more general model [4], [5], [26], which encompasses multiple dielectric waveguides incorporating the beamforming design at the BS. In the proposed model, each PA can independently and dynamically adjust both its spatial positions and allocated transmit-power ratio, while accounting for waveguide propagation losses. As depicted in Fig. 4, the propagation loss between two consecutive PAs, e.g., the m -th and $(m-1)$ -th PA, in the n -th waveguide is denoted as ‘‘PL($d_{n,m-1}^{n,m}$)’’ with their spatial separation $d_{n,m-1}^{n,m} = x_{n,m}^{\text{Pin}} - x_{n,m-1}^{\text{Pin}}$. The power-ratio allocated to the m -th PA in the n -th waveguide

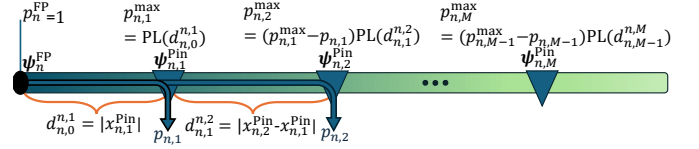


Fig. 4. Illustration of the available power allocation among PAs along the n -th dielectric waveguide considering propagation attenuation.

is denoted by $p_{n,m}$, which can be dynamically managed⁷ as well as its spatial position⁸, subject to constraints $0 \leq x_{n,m}^{\text{Pin}} \leq L$, $d_{n,m-1}^{n,m} \geq \gamma$, where $\gamma > 0$ denotes the minimum allowable spacing among PAs to mitigate coupling effects. Considering lossy dielectric waveguides [1], [26], the maximum available power-ratio at the m -th PA of the n -th waveguide, $\forall n, m$, can be mathematically modeled as follows:

$$p_{n,m}^{\max} = e^{-2\alpha|\psi_n^{\text{FP}} - \psi_{n,m}^{\text{Pin}}|} \left| - \sum_{t=1}^{m-1} p_{n,t} e^{-2\alpha|\psi_{n,m}^{\text{Pin}} - \psi_{n,t}^{\text{Pin}}|} \right|, \quad (11)$$

where $\epsilon_r, \tan(\delta_e), \alpha = \hat{\lambda}\epsilon_r\pi f_c^2 c^{-2} \tan(\delta_e) \in \mathbb{R}^+$ are the dielectric constant, the effective electric loss tangent of the dielectric waveguide, and the attenuation constant [26], [27], respectively. Thus, the maximum allowable power-ratio for each PA depends jointly on its position along the waveguide and the power allocated to preceding PAs.

Furthermore, propagation losses within each waveguide are modeled leveraging a power-ratio vector for each waveguide, $\mathbf{p}_n \in \mathbb{R}^{M \times 1}$, whose entries $\sqrt{p_{n,m}}, \forall n, m$, represent the amplitude-scaling factor applied to the corresponding PA. The transmit power-ratio $p_{n,m}$ is subjected to a maximum value accounting for waveguide propagation loss, denoted by $p_{n,m}^{\max}$, such that the power constraint $p_{n,m} \leq p_{n,m}^{\max}$ holds $\forall n, m$, as shown in (11). Consequently, the introduced model inherently captures critical, non-trivial trade-offs between waveguide propagation losses, the wireless path losses from PAs to users, and power allocation among the PAs. These comprehensive considerations significantly enhance the practical relevance and effectiveness of subsequent resource allocation optimization.

III. PROBLEM STATEMENT

A. Performance Metric

To simplify notation and without loss of generality, an equivalent diagonal power-ratio allocation matrix for all PAs is defined as follows:

$$\mathbf{P} = \text{diag}[\mathbf{p}_1, \dots, \mathbf{p}_N]^\top \in \mathbb{R}^{MN \times N}. \quad (12)$$

⁶Recent studies have demonstrated that in near-field scenarios operating at 28 GHz, the achievable estimation accuracy for 3D position is below 1 cm, while rotation-matrix errors corresponding to angular resolutions better than one degree [38]. Such centimeter-level positioning accuracy and sub-degree orientation estimation justify employing a first-order linear approximation for the orientation perturbation $\Delta\theta_g$ in this work.

⁷In practice, the power-ratio extracted by each PA depends on its coupling length along the dielectric waveguide [6], [41]. To abstract from specific hardware implementations, we assume that PAs dynamically adjust their coupling lengths via an auto-scaling mechanism, enabling precise control of the extracted power-ratio.

⁸Given the small physical length of PAs relative to practical waveguides [26], [41], their impact on propagation loss is neglected.

Consequently, the received signal at user k and EA g are expressed as:

$$r_k = \underbrace{\mathbf{h}_k^H \mathbf{P} \mathbf{w}_k s_k}_{\text{Desired signal}} + \underbrace{\sum_{j' \neq j} \mathbf{h}_k^H \mathbf{P} \mathbf{w}_{j'} s_{j'}}_{\text{Multi-user interference}} + \underbrace{\mathbf{h}_k^H \mathbf{P} \mathbf{v}}_{\text{AN injection}} + \epsilon_k, \forall k, \\ \mathbf{r}_g^E = \mathbf{H}_{E_g}^H \mathbf{P} \mathbf{w}_k s_k + \sum_{j \neq k} \mathbf{H}_{E_g}^H \mathbf{P} \mathbf{w}_j s_j + \mathbf{H}_{E_g}^H \mathbf{P} \mathbf{V} + \epsilon_g, \forall k, g, \quad (13)$$

respectively, where $\epsilon_k \sim \mathcal{CN}(0, \sigma_k^2)$ and $\epsilon_g \sim \mathcal{CN}(\mathbf{0}, \sigma_g^2 \mathbf{I}_T)$ represent the additive white Gaussian noise (AWGN) at user u_k and EA g , respectively, with σ_k^2 and $\sigma_g^2 \mathbf{I}_T$ denoting the corresponding noise power and noise covariance matrix, respectively. Thus, the achievable data rate for user u_k , can be written as:

$$R_k = \log_2 \left(1 + \frac{|\mathbf{h}_k^H \mathbf{P} \mathbf{w}_k|^2}{\sum_{j \neq k} |\mathbf{h}_k^H \mathbf{P} \mathbf{w}_j|^2 + \mathbf{h}_k^H \mathbf{P} \mathbf{V} \mathbf{P}^H \mathbf{h}_k + \sigma_k^2} \right), \forall k. \quad (14)$$

Moreover, from a physical layer security perspective, we consider the worst-case scenario in which potential EAs possess advanced decoding capabilities, allowing them to perfectly remove multi-user interference and attempt to eavesdrop on the signal intended for user k [15], [42]. Thus, the eavesdropping capacity for decoding signal s_k at EA g is given by:

$$R_{k,g}^E = \log_2 \det \left(\mathbf{I}_T + \mathbf{J}_g^{-1} \mathbf{H}_{E_g}^H \mathbf{P} \mathbf{w}_k \mathbf{w}_k^H \mathbf{P}^H \mathbf{H}_{E_g} \right), \forall k, g, \quad (15)$$

where $\mathbf{J}_g = \mathbf{H}_{E_g}^H \mathbf{P} \mathbf{V} \mathbf{P}^H \mathbf{H}_{E_g} + \sigma_g^2 \mathbf{I}_T \succ \mathbf{0}$ represents the interference-plus-noise covariance matrix at EA g , accounting for AN and noise in the worst-case eavesdropping scenario.

B. CSI Error Bound Determination

In this subsection, we derive a geometry-aware Frobenius-norm deterministic upper bound on the CSI error of EA g in (9), $\Delta \mathbf{H}_{E_g} = \mathbf{H}_{E_g} - \hat{\mathbf{H}}_{E_g}$, induced by its position and orientation uncertainties. Noting $\|(\tilde{\mathbf{H}}_{E_g}(\mathbf{E}_g) - \tilde{\mathbf{H}}_{E_g}(\hat{\mathbf{E}}_g)) \odot \tilde{\mathbf{H}}\| \leq \|\tilde{\mathbf{H}}\|_\infty \|\tilde{\mathbf{H}}_{E_g}(\mathbf{E}_g) - \tilde{\mathbf{H}}_{E_g}(\hat{\mathbf{E}}_g)\|_F$, and since $\|\tilde{\mathbf{H}}\|_\infty = 1$ due to the unit-module nature, we establish the following proposition:

Proposition 1: Under the EA location and orientation uncertainty model in (7) and (8), the CSI error of EA g satisfies $\|\Delta \mathbf{H}_{E_g}\|_F \leq \varphi_g^{\text{tot}}$, where:

$$\varphi_g^{\text{tot}} = \frac{\lambda}{4\pi} \sqrt{\sum_{n,m,t} \left(\left[\frac{\Delta \mathbf{R}_g^{(n,m,t)}}{(r_{g,(\text{LB})} - \varphi_g^E)^2} \right]^2 + \frac{2\Omega(\frac{2\pi}{\lambda} \Delta \mathbf{R}_g^{(n,m,t)})}{(r_{g,(\text{LB})} - \varphi_g^E)^2} \right)}, \quad (16)$$

$\Omega(x) \triangleq 1 - \cos x$ if $x < \pi$ and $\Omega(x) \triangleq 2$ otherwise. We denote $\Delta \mathbf{R}_g^{(n,m,t)} \triangleq \varphi_g^E + t\lambda \sin(\frac{\varphi_g^{\text{arc}}}{2}) \left| (\hat{\mathbf{d}}_g^{(n,m,t)})^\top \mathbf{R}_g(\pi/2) \hat{\mathbf{u}}_g \right|$ is the geometry-induced upper bound on $|d - \hat{d}|^2$ obtained by projecting the orientation perturbation onto the LoS direction with $d_g^{(n,m,t)} = \|\mathbf{e}_{g,t} - \psi_{n,m}^{\text{Pin}}\|$, $\hat{d}_g^{(n,m,t)} = \|\hat{\mathbf{e}}_{g,t} - \psi_{n,m}^{\text{Pin}}\|$, and $\hat{\mathbf{d}}_g^{(n,m,t)} \triangleq \frac{\hat{\mathbf{e}}_g + \frac{t\lambda}{2} \hat{\mathbf{u}}_g - \psi_{n,m}^{\text{Pin}}}{\hat{r}} \in \mathbb{R}^2$, where the nominal distance

lower bound is given by:

$$r_{g,(\text{LB})}^{(n,m,t)} = \left[\left(\left\| \hat{\mathbf{u}}_g (\hat{\mathbf{e}}_g + \frac{t\lambda}{2} \hat{\mathbf{u}}_g - \psi_{n,m}^{\text{Pin}}) \right\| - \frac{t\lambda}{2} \left(1 - \cos \left(\frac{\pi}{180} \varphi_g^{\text{arc}} \right) \right) \right)_+ \right]^2 + \left(\left\| (\mathbf{R}_g(\pi/2) \hat{\mathbf{u}}_g)^\top (\hat{\mathbf{e}}_g + \frac{t\lambda}{2} \hat{\mathbf{u}}_g - \psi_{n,m}^{\text{Pin}}) \right\| - \frac{t\lambda}{2} \sin \left(\frac{\pi}{180} \varphi_g^{\text{arc}} \right) \right)_+ \right]^2. \quad (17)$$

Proof. A straightforward expansion of the uncertainty of each link from a PA to an EA antenna yields:

$$\Gamma_g^{(n,m,t)} = \left| \frac{e^{-j \frac{2\pi}{\lambda} d_g^{(n,m,t)}}}{d_g^{(n,m,t)}} - \frac{e^{-j \frac{2\pi}{\lambda} \hat{d}_g^{(n,m,t)}}}{\hat{d}_g^{(n,m,t)}} \right|^2 = \left(\frac{1}{d_g^{(n,m,t)}} - \frac{1}{\hat{d}_g^{(n,m,t)}} \right)^2 + \frac{2(1 - \cos(\frac{2\pi}{\lambda} (d_g^{(n,m,t)} - \hat{d}_g^{(n,m,t)}))}{d_g^{(n,m,t)} \hat{d}_g^{(n,m,t)}}, \quad (18)$$

therefore

$$\left\| \tilde{\mathbf{H}}_{E_g}(\mathbf{E}_g) - \tilde{\mathbf{H}}_{E_g}(\hat{\mathbf{E}}_g) \right\|_F = \frac{\lambda \sqrt{\sum_{n,m,t} \Gamma_g^{(n,m,t)}}}{4\pi}. \quad (19)$$

From the geometry in Fig. 2 and the uncertainty bounds in (7) and (8), the link distance satisfy $|d_g^{(n,m,t)} - \hat{d}_g^{(n,m,t)}| \leq \Delta \mathbf{R}_g^{(n,m,t)}$ and $d_g^{(n,m,t)}, \hat{d}_g^{(n,m,t)} \geq r_{g,(\text{LB})}^{(n,m,t)} - \varphi_g^E$. Substituting these inequalities into (18) and using the definition of the function $\Omega(x)$. Hence, summing over all (n, m, t) yields the channel uncertainty upper bounds in (16). \square

Thus, Proposition 1 converts the coupled EA position-and-orientation uncertainties in (10) into a single tractable Frobenius-norm bound. In this regard, we will directly adopt (16) incorporated into the robust secrecy-rate maximization problem in Section III-C.

C. Problem Formulation

We aim to maximize the sum of achievable rates for legitimate users⁹ while explicitly constraining the amount of information that EAs can decode. To this end, the joint optimization problem over the beamforming for the information signal and AN, the PA positions, and the individual PA power-ratio allocations is formulated as:

$$\mathbf{v} \succeq \mathbf{0} \in \mathbb{H}^N, \mathbf{w}_k, \mathbf{x}_n^{\text{Pin}}, \mathbf{P} \quad \sum_{k \in \mathcal{K}} \min \{R_k\}$$

$$\text{s.t. (C1)} : 0 \leq x_{n,m}^{\text{Pin}} \leq L, \forall n, m,$$

$$\text{(C2)} : x_{n,m+1}^{\text{Pin}} - x_{n,m}^{\text{Pin}} \geq \gamma, \forall n, m \in \{1, \dots, M-1\},$$

$$\text{(C3)} : (\mathbf{s}_{n,m}^{\text{C3}})^\top \mathbf{p}_n \leq e^{-2\alpha} \|\psi_n^{\text{FP}} - \psi_{n,m}^{\text{Pin}}\|, \forall n, m,$$

$$\text{(C4)} : \sum_{k=1}^K |w_{k,n}|^2 + \text{Tr}(\mathbf{V} \mathbf{E}_n) \leq P_n^{\text{max}}, \forall n,$$

$$\text{(C5)} : \sum_{n=1}^N P_n^{\text{max}} \leq P_{\text{max}},$$

⁹Note the proposed formulation, which incorporates information leakage constraints offers a higher flexibility for resource allocation than the direct maximization of the secrecy rate with respect to the heterogeneous secrecy requirement of different applications [15], [24]. Specifically, the information leakage parameter $R_{k,g}^{\text{th}}$, which allows the system operator to strike a balance between the system sum rate and the system secrecy rate.

$$(C6) : \max_{\Delta \mathbf{H}_{E_g} \in \Psi_g^E} R_{k,g}^E \leq R_{k,g}^{\text{th}}, \quad \forall k, g, \quad (20)$$

where $\mathbf{s}_{n,m}^{C3} \in \mathbb{R}^{M \times 1}$ is a predefined power-selection vector for the PA m on the waveguide n . Specifically, $[\mathbf{s}_{n,m}^{C3}]_i = 1, \forall i = m$, $[\mathbf{s}_{n,m}^{C3}]_i = e^{-2\alpha \|\psi_{n,m}^{\text{Pin}} - \psi_{n,i}^{\text{Pin}}\|}, \forall 1 \leq i < m$, and $[\mathbf{s}_{n,m}^{C3}]_i = 0, \forall i > m$. Constraints (C1) and (C2) ensure that PA positions remain within the physical waveguide and maintain the minimum spacing γ between adjacent PAs, respectively, for mitigating mutual potential coupling effects [43]. Besides, constraint (C3) limits the allocated power-ratio $p_{n,m}$ of each PA to its maximum allowable value determined by the propagation attenuation and power-splitting model described previously. Furthermore, constraints (C4) and (C5) ensure that the total allocated power for each waveguide and across all waveguides does not exceed the available power budget for each waveguide P_n^{max} and the proposed system P_{max} , respectively. Finally, constant $R_{k,g}^{\text{th}}$ in constraint (C6) imposes an upper bound on the information leakage to EAs under worst-case CSI uncertainty, explicitly incorporating estimation imperfections. Indeed, problem (20) is inherently nonconvex due to the strong coupling among variables. Hence, we adopt a BCD scheme that alternately optimizes the blocks $\{\mathbf{W}_k, \mathbf{V}, \mathbf{P}\}$ and $\{\mathbf{x}_n^{\text{Pin}}\}$ to obtain a high-quality suboptimal solution.

IV. SOLUTION FOR JOINT OPTIMIZATION OF \mathbf{w}_k, \mathbf{V} AND \mathbf{P}

In this section, we address the first subproblem of our proposed BCD framework, which can be formulated as:

$$\underset{\mathbf{V} \in \mathbb{H}^N, \mathbf{w}_k, \mathbf{P}}{\text{maximize}} \sum_{k \in \mathcal{K}} \min_{\Delta \mathbf{h}_k \in \Psi_k} \{R_k\} \quad \text{s.t. (C3) - (C6)}. \quad (21)$$

The problem in (21) remains nonconvex due to the quadratic coupling among the optimization variables, together with the infinitely many uncertainty-induced constraints, originating from the fractional rate expression and constraint (C6).

A. Problem Transformation

To address the nonconvexity in the objective function of (21), we first introduce $\mathbf{W}_k = \mathbf{w}_k \mathbf{w}_k^H, \forall k$, and then establish a commonly adopted performance lower bound [24], as:

$$\begin{aligned} & \min_{\|\Delta \mathbf{h}_k\| \leq \varphi_k} \left\{ \log_2 \left(1 + \frac{\mathbf{h}_k^H \mathbf{P} \mathbf{W}_k \mathbf{P}^H \mathbf{h}_k}{\sum_{j \neq k} \mathbf{h}_k^H \mathbf{P} \mathbf{W}_j \mathbf{P}^H \mathbf{h}_k + \mathbf{h}_k^H \mathbf{P} \mathbf{V} \mathbf{P}^H \mathbf{h}_k + \sigma_k^2} \right) \right\} \\ & \geq \log_2 \left(1 + \frac{\min_{\|\Delta \mathbf{h}_k\| \leq \varphi_k} \{ \mathbf{h}_k^H \mathbf{P} \mathbf{W}_k \mathbf{P}^H \mathbf{h}_k \}}{\max_{\|\Delta \mathbf{h}_k\| \leq \varphi_k} \left\{ \sum_{j \neq k} \mathbf{h}_k^H \mathbf{P} \mathbf{W}_j \mathbf{P}^H \mathbf{h}_k + \mathbf{h}_k^H \mathbf{P} \mathbf{V} \mathbf{P}^H \mathbf{h}_k + \sigma_k^2 \right\}} \right). \quad (22) \end{aligned}$$

By leveraging logarithmic identities and introducing slack variables l_k^N and l_k^D , the objective lower bound in (22) can be equivalently rewritten in a difference-of-convex (DC) form as:

$$\begin{aligned} & \sum_{k \in \mathcal{K}} \log_2(l_k^N + l_k^D + \sigma_k^2) - \sum_{k \in \mathcal{K}} \log_2(l_k^D + \sigma_k^2) \quad \text{s.t.} \\ (C7): & l_k^N + \max_{\|\Delta \mathbf{h}_k\| \leq \varphi_k} \left\{ -(\hat{\mathbf{h}}_k + \Delta \mathbf{h}_k)^H \mathbf{P} \mathbf{W}_k \mathbf{P}^H (\hat{\mathbf{h}}_k + \Delta \mathbf{h}_k) \right\} \leq 0, \forall k, \end{aligned}$$

$$(C8): \max_{\|\Delta \mathbf{h}_k\| \leq \varphi_k} \left\{ \sum_{j \neq k} (\hat{\mathbf{h}}_k + \Delta \mathbf{h}_k)^H \mathbf{P} \mathbf{W}_j \mathbf{P}^H (\hat{\mathbf{h}}_k + \Delta \mathbf{h}_k) \right\}$$

$$+ (\hat{\mathbf{h}}_k + \Delta \mathbf{h}_k)^H \mathbf{P} \mathbf{V} \mathbf{P}^H (\hat{\mathbf{h}}_k + \Delta \mathbf{h}_k) \leq l_k^D, \forall k,$$

$$(C9) : \mathbf{W}_k \succeq \mathbf{0}, \forall k, \forall k, \quad (C10) : \mathbf{W}_k = \mathbf{w}_k \mathbf{w}_k^H, \forall k, \quad (23)$$

Moreover, constraint (C6) is highly nonconvex, owing to the quadratic coupling of optimization variables and the presence of infinitely many inequality constraints arising from the corresponding CSI uncertainty sets. To overcome this difficulty, we convert it into a tractable form through linear matrix inequalities (LMIs) by defining $\hat{R}_g^{\text{th}} = 2^{R_g^{\text{th}} - 1}$ and introducing the following proposition and equivalent transformation:

Proposition 2: Since $\mathbf{J}_g^{-\frac{1}{2}} \mathbf{H}_{E_g}^H \mathbf{P} \mathbf{W}_k \mathbf{P}^H \mathbf{H}_{E_g} \mathbf{J}_g^{-\frac{1}{2}}$ is a rank-one matrix, constraint (C6) in (20) can be equivalently transformed as:

$$(C6) \Leftrightarrow \max_{\|\Delta \mathbf{H}_{E_g}\|_F \leq \varphi_g^{\text{tot}}} \mathbf{H}_{E_g}^H \mathbf{P} \mathbf{W}_k \mathbf{P}^H \mathbf{H}_{E_g} - \hat{R}_{k,g}^{\text{th}} \left(\mathbf{H}_{E_g}^H \mathbf{P} \mathbf{V} \mathbf{P}^H \mathbf{H}_{E_g} + \sigma_g^2 \mathbf{I}_T \right) \preceq \mathbf{0}, \forall k, g. \quad (24)$$

Proof. According to Sylvester's determinant identity $\det(\mathbf{I} + \mathbf{A}\mathbf{B}) = \det(\mathbf{I} + \mathbf{B}\mathbf{A})$ [15], [24], we have

$$\begin{aligned} & \max_{\Delta \mathbf{H}_{E_g} \in \Psi_g^E} \log_2 \det \left(\mathbf{I}_T + \mathbf{J}_g^{-1} \mathbf{H}_{E_g}^H \mathbf{P} \mathbf{W}_k \mathbf{w}_k^H \mathbf{P}^H \mathbf{H}_{E_g} \right) \leq R_{k,g}^{\text{th}} \\ & \Leftrightarrow \max_{\Delta \mathbf{H}_{E_g} \in \Psi_g^E} \log_2 \left(1 + \mathbf{w}_k^H \mathbf{P}^H \mathbf{H}_{E_g} \mathbf{J}_g^{-1} \mathbf{H}_{E_g}^H \mathbf{P} \mathbf{W}_k \right) \leq R_{k,g}^{\text{th}} \\ & \Leftrightarrow \max_{\Delta \mathbf{H}_{E_g} \in \Psi_g^E} \text{Tr} \left(\mathbf{J}_g^{-1} \mathbf{H}_{E_g}^H \mathbf{P} \mathbf{W}_k \mathbf{w}_k^H \mathbf{P}^H \mathbf{H}_{E_g} \right) \leq \hat{R}_{k,g}^{\text{th}} \\ & \stackrel{(a)}{\Leftrightarrow} \max_{\Delta \mathbf{H}_{E_g} \in \Psi_g^E} \lambda_{\max} \left(\mathbf{J}_g^{-1/2} \mathbf{H}_{E_g}^H \mathbf{P} \mathbf{W}_k \mathbf{w}_k^H \mathbf{P}^H \mathbf{H}_{E_g} \mathbf{J}_g^{-1/2} \right) \leq \hat{R}_{k,g}^{\text{th}} \\ & \Leftrightarrow \max_{\Delta \mathbf{H}_{E_g} \in \Psi_g^E} \left(\mathbf{H}_{E_g}^H \mathbf{P} \mathbf{W}_k \mathbf{w}_k^H \mathbf{P}^H \mathbf{H}_{E_g} - (2^{R_{k,g}^{\text{th}}} - 1) \mathbf{J}_g \right) \preceq \mathbf{0}, \quad (25) \end{aligned}$$

where (a) holds since the matrix $\mathbf{J}_g^{-1} \mathbf{H}_{E_g}^H \mathbf{P} \mathbf{W}_k \mathbf{w}_k^H \mathbf{P}^H \mathbf{H}_{E_g}$ is rank one, and thus its largest eigenvalue equals its sole nonzero eigenvalue. Substituting the definition of \mathbf{J}_g into the last matrix inequality of (15) yields Proposition 2. \square

Although (C6) still comprises infinitely many constraints, its LMI reformulation in (24) substantially improves tractability. To further handle the quadratic coupling between $\{\mathbf{P}, \mathbf{W}_k\}$ and $\{\mathbf{P}, \mathbf{V}\}$, we recast (C6) as:

$$(\overline{C6}): \max_{\|\Delta \mathbf{H}_{E_g}\|_F \leq \varphi_g^{\text{tot}}} \mathbf{H}_{E_g}^H \mathbf{Y}_k \mathbf{H}_{E_g} - \hat{R}_g^{\text{th}} \left(\mathbf{H}_{E_g}^H \mathbf{Z} \mathbf{H}_{E_g} + \sigma_g^2 \mathbf{I}_T \right) \preceq \mathbf{0}, \forall k, g,$$

$$(C11): \mathbf{y}_k = \mathbf{P} \mathbf{w}_k, \mathbf{Y}_k = \mathbf{y}_k \mathbf{y}_k^H, \forall k,$$

$$(C12): \mathbf{z} = \mathbf{P} \mathbf{v}, \mathbf{Z} = \mathbf{z} \mathbf{z}^H, \quad (C13): \mathbf{V} = \mathbf{v} \mathbf{v}^H. \quad (26)$$

Noting that new equality constraints induce nonconvexity, we adopt the Schur complement following [24], [44]. Taking $\mathbf{y}_k = \mathbf{P} \mathbf{w}_k$ as an example, it can be equivalently represented as:

$$(C11a): \begin{bmatrix} \mathbf{U}_k & \mathbf{y}_k & \mathbf{P} \\ \mathbf{y}_k^H & s_k & \mathbf{w}_k^H \\ \mathbf{P}^H & \mathbf{w}_k & \mathbf{I}_N \end{bmatrix} \succeq \mathbf{0}, \forall k,$$

$$(C11b): \text{Tr}(\mathbf{U}_k - \mathbf{P} \mathbf{P}^H) \leq 0, \forall k, \quad (C11c): \mathbf{U}_k \succeq \mathbf{0}, s_k \geq 0, \forall k, \quad (27)$$

where $\mathbf{U}_k \in \mathbb{C}^{MN \times MN}$ and s_k are slack optimization variables. Moreover, the other nonconvex equality in (C11), $\mathbf{Y}_k = \mathbf{y}_k \mathbf{y}_k^H$, can be replaced by the following two constraints [24],

as:

$$(C11d): \mathcal{Y}_k = \begin{bmatrix} \mathbf{Y}_k & \mathbf{y}_k \\ \mathbf{y}_k^H & 1 \end{bmatrix} \succeq \mathbf{0}, \forall k, (C11e): \text{Rank}(\mathcal{Y}_k) = 1, \forall k. \quad (28)$$

Following the same structure, constraints (C10), (C12), and (C13) can be equivalently written as:

$$(C10a): \mathcal{W}_k = \begin{bmatrix} \mathbf{W}_k & \mathbf{w}_k \\ \mathbf{w}_k^H & 1 \end{bmatrix} \succeq \mathbf{0}, \forall k, (C10b): \text{Rank}(\mathcal{W}_k) = 1, \forall k,$$

$$(C12a): \begin{bmatrix} \bar{\mathbf{U}} & \mathbf{z} & \mathbf{P} \\ \mathbf{z}^H & \bar{s} & \mathbf{v}^H \\ \mathbf{P}^H & \mathbf{v} & \mathbf{I}_N \end{bmatrix} \succeq \mathbf{0}, (C12b): \text{Tr}(\bar{\mathbf{U}} - \mathbf{P}\mathbf{P}^H) \leq 0,$$

$$(C12c): \bar{\mathbf{U}} \succeq \mathbf{0}, \bar{s} \geq 0, (C12d): \mathcal{Z} = \begin{bmatrix} \mathbf{Z} & \mathbf{z} \\ \mathbf{z}^H & 1 \end{bmatrix} \succeq \mathbf{0},$$

$$(C12e): \text{Rank}(\mathcal{Z}) = 1,$$

$$(C13a): \mathcal{V} = \begin{bmatrix} \mathbf{V} & \mathbf{v} \\ \mathbf{v}^H & 1 \end{bmatrix} \succeq \mathbf{0}, (C13b): \text{Rank}(\mathcal{V}) = 1. \quad (29)$$

With the transformation in (27)-(29), the constraint sets (C11a) through (C11d) and (C12a) through (C12d) enforce the relations $\mathbf{Y}_k = \mathbf{P}\mathbf{W}_k\mathbf{P}^H, \forall k$, and $\mathbf{Z} = \mathbf{P}\mathbf{V}\mathbf{P}^H$, respectively. These relations permit the direct substitution of \mathbf{Y}_k and \mathbf{Z} for $\mathbf{P}\mathbf{W}_k\mathbf{P}^H$ and $\mathbf{P}\mathbf{V}\mathbf{P}^H$ in constraints (C7) and (C8) in (23), thereby eliminating the explicit quadratic coupling in those constraints.

Note that (C9) can be omitted since (C10a) always ensures $\mathbf{W}_k \succeq \mathbf{0}$. The nonconvexity due to coupling has been transformed into a series of convex constraints, except the DC-formatted constraints (C11b) and (C12b) and the nonconvex rank-one constraints. Hence, a performance lower bound of problem (21) can be obtained by solving the following optimization problem:

$$\begin{aligned} & \underset{\substack{\mathbf{W}_k, \mathbf{V} \in \mathbb{H}^N, \mathcal{V} \in \mathbb{H}^{N+1}, \\ \mathcal{Y}_k, \mathcal{W}_k, \mathcal{Z} \in \mathbb{H}^{MN+1}, \mathbf{P}, \mathbf{w}_k, \\ \iota_k^N, \iota_k^D, \mathbf{U}_k, \bar{\mathbf{U}}, s_k, \bar{s}, \mathbf{v}, \mathbf{Y}_k, \mathbf{y}_k, \mathbf{Z}, \mathbf{z}}}{\text{maximize}} \sum_{k \in \mathcal{K}} (\log_2(\iota_k^N + \iota_k^D + \sigma_k^2) - \log_2(\iota_k^D + \sigma_k^2)) \\ \text{s.t. } & (C3) - (C5), \overline{(C6)}, (C7), (C8), (C10a), (C10b), \\ & (C11a) - (C12e), (C13a), \text{ and } (C13b). \end{aligned} \quad (30)$$

B. S-Procedure

To handle the infinitely many possibilities arising in constraints (C6), (C7b), and (C8b), we introduce the following two Lemmas [15], [24]:

Lemma 1. (Standard S-Procedure [24]): Let a function $f_m(\mathbf{x}), m \in \{1, 2\}$, be defined as:

$$f_m(\mathbf{x}) = \mathbf{x}^H \mathbf{C}_m \mathbf{x} + 2\text{Re}\{\mathbf{c}_m^H \mathbf{x}\} + c_m, \quad (31)$$

where $\mathbf{C}_m \in \mathbb{H}^N, \mathbf{c}_m \in \mathbb{C}^{N \times 1}$, and $c_m \in \mathbb{R}^{1 \times 1}$. Then, the implication $f_1(\mathbf{x}) \leq 0 \Rightarrow f_2(\mathbf{x})$ holds if and only if there exists a $\delta \geq 0$ such that

$$\delta \begin{bmatrix} \mathbf{C}_1 & \mathbf{c}_1 \\ \mathbf{c}_1^H & c_1 \end{bmatrix} - \begin{bmatrix} \mathbf{C}_2 & \mathbf{c}_2 \\ \mathbf{c}_2^H & c_2 \end{bmatrix} \succeq \mathbf{0}. \quad (32)$$

Lemma 2. (Generalized S-Procedure [15]): Let a function $f(\mathbf{X})$ defined as:

$$f(\mathbf{X}) = \mathbf{X}^H \mathbf{A} \mathbf{X} + \mathbf{X}^H \mathbf{B} + \mathbf{B}^H \mathbf{X} + \mathbf{C}, \quad (33)$$

where $\mathbf{X}, \mathbf{B} \in \mathbb{C}^{MN \times MM}, \mathbf{A} \in \mathbb{H}^{MN}, \mathbf{C} \in \mathbb{C}^{M \times M}$, and $\mathbf{D} \succeq \mathbf{0} \in \mathbb{C}^{MN \times MN}$. There exists a $\delta \geq 0$ such that $f(\mathbf{X}) \succeq 0, \forall \mathbf{X} \in \{\mathbf{X} | \text{Tr}(\mathbf{D}\mathbf{X}\mathbf{X}^H) \leq 1\}$ is equivalent to

$$\begin{bmatrix} \mathbf{C} & \mathbf{B}^H \\ \mathbf{B} & \mathbf{A} \end{bmatrix} - \delta \begin{bmatrix} \mathbf{I}_M & \mathbf{0} \\ \mathbf{0} & -\mathbf{D} \end{bmatrix} \succeq \mathbf{0}. \quad (34)$$

With defining $\bar{\mathbf{Z}}_k = \sum_{j \neq k} \mathbf{Y}_j + \mathbf{Z}$, constraints (C7) and (C8b) can be equivalently recast by adopting Lemma 1, as:

$$\overline{(C7a)}: \begin{bmatrix} \mathbf{Y}_k + \delta_k^{C7} \mathbf{I}_{MN} & \mathbf{Y}_k \hat{\mathbf{h}}_k \\ \hat{\mathbf{h}}_k^H \mathbf{Y}_k & \hat{\mathbf{h}}_k^H \mathbf{Y}_k \hat{\mathbf{h}}_k - \delta_k^{C7} \varrho_k^2 - \iota_k^N \end{bmatrix} \succeq \mathbf{0}, \forall k,$$

$$\overline{(C8a)}: \begin{bmatrix} \delta_k^{C8} \mathbf{I}_{MN} - \bar{\mathbf{Z}}_k & -\bar{\mathbf{Z}}_k \hat{\mathbf{h}}_k \\ -\hat{\mathbf{h}}_k^H \bar{\mathbf{Z}}_k & \iota_k^D - \delta_k^{C8} \varrho_k^2 - \hat{\mathbf{h}}_k^H \bar{\mathbf{Z}}_k \hat{\mathbf{h}}_k \end{bmatrix} \succeq \mathbf{0}, \forall k,$$

$$\overline{(C7b)}: \delta_k^{C7} \geq 0, \forall k, \quad \overline{(C8b)}: \delta_k^{C8} \geq 0, \forall k, \quad (35)$$

Similarly, we adopt the generalized S-procedure [15] in Lemma 2 to handle constraint (C6), which can be equivalently written with a LMI format, as:

$$\begin{aligned} \overline{(C6a)}: & \begin{bmatrix} (\hat{R}_g^{\text{th}} \sigma_g^2 - \delta_{k,g}^E) \mathbf{I}_T + \hat{\mathbf{H}}_{E_g}^H \mathbf{M}_{k,g}^E \hat{\mathbf{H}}_{E_g} & \hat{\mathbf{H}}_{E_g}^H \mathbf{M}_{k,g}^E \\ \mathbf{M}_{k,g}^E \hat{\mathbf{H}}_{E_g} & \mathbf{M}_{k,g}^E + \frac{\delta_{k,g}^E \mathbf{I}_{LMN}}{(\varphi_g^{\text{tot}})^2} \end{bmatrix} \succeq \mathbf{0}, \forall k, g, \\ \overline{(C6b)}: & \delta_{k,g}^E \geq 0, \forall k, g, \end{aligned} \quad (36)$$

where $\delta_{k,g}^E$ are slack variables and $\mathbf{M}_{k,g}^E = \hat{R}_g^{\text{th}} \mathbf{Z} - \mathbf{Y}_k$. In particular, constraint (C6a) involves only KG LMI constraints, which is significantly more tractable than the original semi-infinite form.

C. MM Procedure

Since the rank-one constraints (C10b), (C11e), (C12e), and (C13b) are nonconvex, we employ a DC reformulation and handle them by adopting an MM procedure. We first present the following lemma, taking (C11e) as an example.

Lemma 3. The rank-one constraints (C11e) are equivalent to constraint (C11e) in a DC format, given by:

$$\overline{(C11e)}: \|\mathcal{Y}_k\|_* - \|\mathcal{Y}_k\|_2 \leq 0, \forall k. \quad (37)$$

Proof. For any $\mathbf{X} \in \mathbb{H}^n \succeq \mathbf{0}$, the inequality $\|\mathbf{X}\|_* = \sum_i x_i \geq \|\mathbf{X}\|_2 = \max\{x_i\}$ holds, where x_i is the i -th singular value of \mathbf{X} . Equality holds if and only if \mathbf{X} is rank-one. \square

Following the same approach, the rank-one constraints (C10b), (C12e), and (C13b) can also be expressed in DC form. With these transformations, all remaining sources of nonconvexity of the constraints and objective arises solely from their DC structure. Hence, we adopt an MM scheme based on first-order Taylor linearization and introduce the following propositions.

Proposition 3. For the convex function $-\sum_{k \in \mathcal{K}} \log_2(\iota_k^D + \sigma_k^2)$,

an affine lower bound $\bar{R}(l_k^{\text{D}(i_1)})$ can be established at any given feasible $l_k^{\text{D}(i_1)}$ in the (i_1+1) -th iteration of the MM, as:

$$\begin{aligned} & - \sum_{k \in \mathcal{K}} \log_2(l_k^{\text{D}} + \sigma_k^2) \geq \bar{R}(l_k^{\text{D}(i_1)}) \\ \triangleq & - \sum_{k \in \mathcal{K}} \log_2(l_k^{\text{D}(i_1)} + \sigma_k^2) - \sum_{k \in \mathcal{K}} \frac{1}{\ln 2} \frac{l_k^{\text{D}} - l_k^{\text{D}(i_1)}}{l_k^{\text{D}(i_1)} + \sigma_k^2}. \end{aligned} \quad (38)$$

Proposition 4. For the convex quadratic term $\text{Tr}(\mathbf{X}^H \mathbf{X})$, an affine global lower bound, $\bar{L}(\mathbf{X}^{(i_1)})$, can be established at any given feasible point $\mathbf{X}^{(i_1)}$ in the (i_1+1) -th iteration of the MM, as:

$$\text{Tr}(\mathbf{X}^H \mathbf{X}) \geq \bar{L}(\mathbf{X}^{(i_1)}) \triangleq - \left\| \mathbf{X}^{(i_1)} \right\|_F^2 + 2\text{Tr} \left((\mathbf{X}^{(i_1)})^H \mathbf{X} \right). \quad (39)$$

Proposition 5. For the DC rank-one surrogate $\|\mathbf{X}\|_* - \|\mathbf{X}\|_2 \leq 0$ with $\mathbf{X} \in \mathbb{H}^n \succeq \mathbf{0}$, a convex subset can be established at any given feasible local point $\mathbf{X}^{(i_1)}$ in the (i_1+1) -th iteration of the MM, denoted as:

$$\|\mathbf{X}\|_* - \text{Tr} \left[\lambda_{\max}(\mathbf{X}^{(i_1)}) \lambda_{\max}^H(\mathbf{X}^{(i_1)}) (\mathbf{X} - \mathbf{X}^{(i_1)}) \right] - \|\mathbf{X}^{(i_1)}\|_2 \leq 0. \quad (40)$$

By adopting Proposition 4, a lower bound for $\text{Tr}(\mathbf{P}\mathbf{P}^H)$ can be obtained. Therefore, subsets of the related non-convex constraint sets are given by:

$$\begin{aligned} (\overline{\text{C11b}}) : & \text{Tr}(\mathbf{U}_k) + \left\| \mathbf{P}^{(i_1)} \right\|_F^2 - 2\text{Tr} \left((\mathbf{P}^{(i_1)})^H \mathbf{P} \right) \leq 0, \forall k, \\ (\overline{\text{C12b}}) : & \text{Tr}(\bar{\mathbf{U}}) + \left\| \mathbf{P}^{(i_1)} \right\|_F^2 - 2\text{Tr} \left((\mathbf{P}^{(i_1)})^H \mathbf{P} \right) \leq 0, \end{aligned} \quad (41)$$

respectively. All remaining DC-form rank-one constraints $(\overline{\text{C10b}})$, $(\overline{\text{C12e}})$, and $(\overline{\text{C13b}})$ follow directly from the Proposition 5; details are omitted due to page limits. Here, $(\overline{\text{C10b}}) \Rightarrow (\overline{\text{C10b}})$, $(\overline{\text{C11b}}) \Rightarrow (\text{C11b})$, $(\overline{\text{C11e}}) \Rightarrow (\overline{\text{C11e}})$, $(\overline{\text{C12b}}) \Rightarrow (\text{C12b})$, $(\overline{\text{C12e}}) \Rightarrow (\overline{\text{C12e}})$, and $(\overline{\text{C13b}}) \Rightarrow (\overline{\text{C13b}})$.

For notational simplicity, we define $\iota = \{l_k^{\text{N}}, l_k^{\text{D}}\}$ and $\delta = \{\delta_k^{\text{C7}}, \delta_k^{\text{C8}}, \delta_{k,g}^{\text{E}}\}$, and. Thus, a lower bound of (21) is obtained by solving the following optimization problem in the (i_1+1) -th MM iteration:

$$\begin{aligned} & \underset{\substack{\mathbf{W}_k, \mathbf{V} \in \mathbb{H}^N, \mathcal{V} \in \mathbb{H}^{N+1}, \\ \mathcal{Y}_k, \mathcal{W}_k, \mathcal{Z} \in \mathbb{H}^{MN+1}, \mathbf{w}_k, \\ \delta, \iota, \mathbf{U}_k, \bar{\mathbf{U}}, \mathbf{s}_k, \bar{\mathbf{s}}, \mathbf{v}, \mathbf{Y}_k, \mathbf{Z}, \mathbf{z}}}{\text{maximize}} \sum_{k \in \mathcal{K}} \log_2(l_k^{\text{N}} + l_k^{\text{D}} + \sigma_k^2) + \bar{R}(l_k^{\text{D}(i_1)}) \\ \text{s.t.} & (\text{C3}) - (\text{C5}), (\overline{\text{C6a}}), (\overline{\text{C6b}}), (\overline{\text{C7a}}), (\overline{\text{C7b}}), (\overline{\text{C8a}}), \\ & (\overline{\text{C8b}}), (\text{C10a}), (\overline{\text{C10bb}}), (\text{C11a}), (\overline{\text{C11b}}), (\text{C11c}) \\ & (\text{C11d}), (\overline{\text{C11e}}), (\text{C12a}), (\overline{\text{C12b}}), (\text{C12c}), (\text{C12d}), \\ & (\overline{\text{C12e}}), (\text{C13a}), \text{ and } (\overline{\text{C13b}}). \end{aligned} \quad (42)$$

Note that the optimization problem in (42) is convex and can be solved by adopting standard numerical solver for convex programming.

V. PA LOCATION SOLUTION

With fixed \mathbf{w}_k , \mathbf{V} , and \mathbf{P} , the PA-positioning subproblem is:

$$\underset{\mathbf{x}_n^{\text{Pin}}}{\text{maximize}} \sum_{k \in \mathcal{K}} \min_{\|\Delta \mathbf{h}_k\| \leq \varphi_k} R_k \text{ s.t. } (\text{C1}), (\text{C2}), \text{ and } (\text{C6}). \quad (43)$$

In fact, the PA locations simultaneously affect phase shifts, path loss, and blockage-induced channel coefficients, so these position-dependent terms are tightly coupled, making (43) challenging to handle directly. To facilitate the presentation in the sequel, we decompose the PA-dependent channel into three separate components. Specifically, we define the pathloss and phase shift vectors as $\mathbf{f}_{n,u_k} = \left[\frac{1}{\|\phi_k - \psi_{n,1}^{\text{Pin}}\|}, \dots, \frac{1}{\|\phi_k - \psi_{n,M}^{\text{Pin}}\|} \right]^T \in \mathbb{R}^{M \times 1}$ and $\mathbf{a}_{n,u_k}^H = \left[e^{-j\theta_{n,1,k}}, \dots, e^{-j\theta_{n,M,k}} \right] \in \mathbb{C}^{1 \times M}$, $\forall n, k$, respectively, where $\theta_{n,m,k} = \frac{2\pi}{\lambda} \|\phi_k - \psi_{n,m}^{\text{Pin}}\| + \frac{2\pi}{\lambda} \|\psi_{n,m}^{\text{FP}} - \psi_{n,m}^{\text{Pin}}\|$, $\forall n, m, k$. We further define $\mathbf{a}_k^H = [\mathbf{a}_{1,u_k}^H, \dots, \mathbf{a}_{N,u_k}^H] \in \mathbb{C}^{1 \times MN}$ and $\mathbf{f}_k = \text{vec}([\mathbf{f}_{1,u_k}, \dots, \mathbf{f}_{N,u_k}]) \in \mathbb{R}^{MN \times 1}$. The blockage-impacted channel-coefficient vector for user u_k is denoted by $\mathbf{c}_k \in \mathbb{R}^{MN \times 1}$, where the $l(n, m)$ -th element of \mathbf{c}_k is $\sqrt{\eta_k^{n,m}}$ and $l(n, m) = (n-1)M + m$. Similarly, we apply the same decomposition for each EA and characterize its path loss, phase shift, and blockage-impacted coefficients by $\mathbf{f}_g^{\text{E}} \in \mathbb{R}^{MNT \times 1}$, $\mathbf{a}_g^{\text{E}} \in \mathbb{C}^{MNT \times 1}$, and $\mathbf{c}_g^{\text{E}} \in \mathbb{C}^{MNT \times 1}$, respectively. Hence, the nominal channels can be written as $\hat{\mathbf{h}}_k = \mathbf{c}_k \odot \mathbf{a}_k \odot \mathbf{f}_k$, $\forall k$, and $\text{vec}(\hat{\mathbf{H}}_g^{\text{E}}) = \mathbf{c}_g^{\text{E}} \odot \mathbf{a}_g^{\text{E}} \odot \mathbf{f}_g^{\text{E}}$, $\forall g$.

Although the above factorization decouples the channel structure, all three terms still depend on the same PA positions but operate on different physical scales: meter-level displacements mainly affect path loss and blockage-impacted channel coefficients, whereas wavelength-level displacements primarily tune the phases. Motivated by this scale separation, we adopt a two-stage PA positioning strategy. In the first stage, we determine a coarse large-scale PA placement dominated by path loss and blockage effects while keeping the phase terms fixed. In the second stage, starting from this coarse solution, we refine $\mathbf{x}_n^{\text{Pin}}$ within a few wavelengths to improve phase alignment and array gain. This separation significantly reduces the problem complexity while remaining physically meaningful. In both stages, we employ the transformations in (22) and (23) together with $\mathbf{Y}_k = \mathbf{P}\mathbf{W}_k\mathbf{P}^H$ and $\mathbf{Z} = \mathbf{P}\mathbf{V}\mathbf{P}^H$ to obtain tractable performance lower bounds under constraints (C7) and (C8) in (23). Hence, a lower bound of the problem in (43) can be represented as:

$$\begin{aligned} & \underset{\substack{l_k^{\text{N}}, l_k^{\text{D}}, \hat{\mathbf{h}}_k, \mathbf{h}_k \\ \mathbf{a}_k \mathbf{f}_k, \mathbf{c}_k, \mathbf{a}_g^{\text{E}}, \mathbf{f}_g^{\text{E}}, \mathbf{c}_g^{\text{E}}}}{\text{maximize}} \sum_{k \in \mathcal{K}} \log_2(l_k^{\text{N}} + l_k^{\text{D}} + \sigma_k^2) - \sum_{k \in \mathcal{K}} \log_2(l_k^{\text{D}} + \sigma_k^2) \\ \text{s.t.} & (\text{C1}), (\text{C2}) \\ (\overline{\text{C6}}) : & \max_{\|\Delta \mathbf{H}_{E_g}\|_F \leq \varrho_g^{\text{tot}}} \mathbf{H}_{E_g}^H \mathbf{Y}_k \mathbf{H}_{E_g} - \hat{R}_g^{\text{th}} \left(\mathbf{H}_{E_g}^H \mathbf{Z} \mathbf{H}_{E_g} + \sigma_g^2 \mathbf{I}_T \right) \leq \mathbf{0}, \forall k, g, \\ (\overline{\text{C7}}) : & l_k^{\text{N}} + \max_{\|\Delta \mathbf{h}_k\| \leq \varphi_k} \left\{ -(\hat{\mathbf{h}}_k + \Delta \mathbf{h}_k)^H \mathbf{Y}_k (\hat{\mathbf{h}}_k + \Delta \mathbf{h}_k) \right\} \leq 0, \forall k, \\ (\overline{\text{C8}}) : & \max_{\|\Delta \mathbf{h}_k\| \leq \varphi_k} \left\{ (\hat{\mathbf{h}}_k + \Delta \mathbf{h}_k)^H \bar{\mathbf{Z}}_k (\hat{\mathbf{h}}_k + \Delta \mathbf{h}_k) \right\} \leq l_k^{\text{D}}, \forall k, \\ (\overline{\text{C9}}) : & \hat{\mathbf{h}}_k = \mathbf{c}_k \odot \mathbf{f}_k \odot \mathbf{a}_k, \forall k, \\ (\overline{\text{C10}}) : & \text{vec}(\hat{\mathbf{H}}_g^{\text{E}}) = \mathbf{c}_g^{\text{E}} \odot \mathbf{f}_g^{\text{E}} \odot \mathbf{a}_g^{\text{E}}, \forall g, \end{aligned} \quad (44)$$

where $\bar{\mathbf{Z}}_k = \sum_{j \neq k} \mathbf{Y}_j + \mathbf{Z}$, $\forall k$. We will iteratively optimize $\{\mathbf{f}_k, \mathbf{c}_k, \mathbf{f}_g^{\text{E}}, \mathbf{c}_g^{\text{E}}, \mathbf{x}_n^{\text{Pin}}, l_k^{\text{N}}, l_k^{\text{D}}\}$ for meter-levels PA positioning and $\{\mathbf{a}_k, \mathbf{a}_g^{\text{E}}, \mathbf{x}_n^{\text{Pin}}, l_k^{\text{N}}, l_k^{\text{D}}\}$ for phase shift-based wavelength-level adjustment.

A. Large Scale Movement with Blockage Effects

In the first stage, we focus on the large-scale movement of the PAs. Since \mathbf{h}_k , \mathbf{f}_k , and \mathbf{a}_k are highly coupled and enter quadratically in (44), we first apply a lifting step for $\mathbf{H}_k = \mathbf{h}_k \mathbf{h}_k^H$, $\mathbf{C}_k = \mathbf{c}_k \mathbf{c}_k^H$, $\mathbf{F}_k = \mathbf{f}_k \mathbf{f}_k^H$, $\forall k$, and fixing the phase-shift matrix as $\mathbf{A}_k^D = \text{diag}(\mathbf{a}_k)$ and $\hat{\mathbf{A}}_k = \mathbf{A}_k^D \odot \text{diag}(\mathbf{P}\mathbf{w}_k^*)$. Then, constraint (C9) is equivalently to:

$$\begin{aligned} (\widetilde{\text{C9a}}): & \text{Tr}(\mathbf{Y}_k \hat{\mathbf{H}}_k) = \text{Tr}(\mathbf{C}_k \hat{\mathbf{A}}_k \mathbf{F}_k \hat{\mathbf{A}}_k^H), \forall k, \\ (\widetilde{\text{C9b}}): & \text{Rank}(\mathbf{C}_k) = 1, \forall k, \quad (\widetilde{\text{C9c}}): \text{Rank}(\mathbf{F}_k) = 1, \forall k, \\ (\widetilde{\text{C9d}}): & \text{Rank}(\mathcal{H}_k) = 1, \forall k, \\ (\widetilde{\text{C9e}}): & \mathcal{H}_k = \begin{bmatrix} \hat{\mathbf{H}}_k & \hat{\mathbf{h}}_k \\ \hat{\mathbf{h}}_k^H & 1 \end{bmatrix} \succeq \mathbf{0} \in \mathbb{C}^{(MN+1) \times (MN+1)}, \forall k. \end{aligned} \quad (45)$$

Moreover, using the transformation in (45) and the known selection matrices $\mathbf{S} = [\mathbf{I}_{MN} \ \mathbf{0}] \in \mathbb{R}^{MN \times (MN+1)}$ and $\mathbf{s} = [\mathbf{0}_{MN} \ 1]^T \in \mathbb{R}^{(MN+1) \times 1}$, constraints (C7) and (C8) in (44) can be equivalently converted by Lemma 1, as following LMIs:

$$\begin{aligned} (\widetilde{\text{C7a}}): & \begin{bmatrix} \mathbf{Y}_k - \delta_k^N \mathbf{I}_{MN} & \mathbf{Y}_k \mathbf{S} \mathcal{H}_k \mathbf{s} \\ \mathbf{s}^H \mathcal{H}_k \mathbf{S}^H \mathbf{Y}_k & \text{Tr}(\mathbf{Y}_k \mathbf{S} \mathcal{H}_k \mathbf{S}^H) - \iota_k^N + \delta_k^N \varrho_k^2 \end{bmatrix} \succeq \mathbf{0}, \forall k, \\ (\widetilde{\text{C8b}}): & \begin{bmatrix} \delta_k^D \mathbf{I}_{MN} - \bar{\mathbf{Z}}_k & -\bar{\mathbf{Z}}_k \mathbf{S} \mathcal{H}_k \mathbf{s} \\ -\mathbf{s}^H \mathcal{H}_k \mathbf{S}^H \bar{\mathbf{Z}}_k & \iota_k^D - \text{Tr}(\bar{\mathbf{Z}}_k \mathbf{S} \mathcal{H}_k \mathbf{S}^H) - \delta_k^D \varrho_k^2 \end{bmatrix} \succeq \mathbf{0}, \forall k, \\ (\widetilde{\text{C7b}}): & \delta_k^N \geq 0, \forall k, \quad (\widetilde{\text{C8a}}): \delta_k^D \geq 0, \forall k, \end{aligned} \quad (46)$$

Then, the only non-convex constraints in (45) and (46) are the rank-one constraints and the equality constraint (C9a).

We next shift our focus to constraint (C6) in (44) with defining $\mathbf{M}_{k,g}^E = \hat{R}_{k,g}^{\text{th}} \mathbf{Z} - \mathbf{Y}_k$, $\mathbf{j}_g = \text{vec}(\hat{\mathbf{H}}_{E_g}) \in \mathbb{C}^{MNT \times 1}$, and $\mathbf{J}_g = \mathbf{j}_g \mathbf{j}_g^H$, $\forall g$. Following the same lifting procedure as for the legitimate users, we set $\mathbf{F}_g^E = \mathbf{f}_g^E (\mathbf{f}_g^E)^H$ and $\mathbf{C}_g^E = \mathbf{c}_g^E (\mathbf{c}_g^E)^H$. We further introduce a known nonzero vector $\bar{\mathbf{m}} \in \mathbb{C}^{MNT \times 1}$ and its rank-one matrix $\bar{\mathbf{M}} = \bar{\mathbf{m}} \bar{\mathbf{m}}^H$ to establish the relationship between \mathbf{j}_g and \mathbf{c}_g^E , \mathbf{f}_g^E , \mathbf{a}_g^E in constraint (C10). By fixing the phase-shift term as $\mathbf{A}_{E_g}^D = \text{diag}(\mathbf{a}_g^E)$ and defining $\hat{\mathbf{A}}_g^E = \mathbf{A}_{E_g}^D \odot \text{diag}(\bar{\mathbf{m}}^*)$, constraint (C10) can be equivalently rewritten as:

$$\begin{aligned} (\widetilde{\text{C10a}}): & \text{Tr}(\bar{\mathbf{M}} \mathbf{J}_g) = \text{Tr}(\mathbf{C}_g^E \hat{\mathbf{A}}_g^E \mathbf{F}_g^E (\hat{\mathbf{A}}_g^E)^H), \forall g, \\ (\widetilde{\text{C10b}}): & \text{Rank}(\mathbf{C}_g^E) = 1, \forall g, \quad (\widetilde{\text{C10c}}): \text{Rank}(\mathbf{F}_g^E) = 1, \forall g, \\ (\widetilde{\text{C10d}}): & \text{Rank}(\mathcal{J}_g) = 1, \forall g, \\ (\widetilde{\text{C10e}}): & \mathcal{J}_g = \begin{bmatrix} \mathbf{J}_g & \mathbf{j}_g \\ \mathbf{j}_g^H & 1 \end{bmatrix} \succeq \mathbf{0} \in \mathbb{C}^{(MNT+1) \times (MNT+1)}, \forall g, k. \end{aligned} \quad (47)$$

Based on the transformation in (47), we define the column selector $\bar{\mathbf{s}}_t \in \mathbb{R}^{T \times 1}$ with $[\bar{\mathbf{s}}_t]_t = 1$ and zeros elsewhere, the selection matrix as $\bar{\mathbf{S}}_t = \bar{\mathbf{s}}_t \otimes \mathbf{I}_{MN} \in \mathbb{R}^{MNT \times MN}$, $\mathcal{S}_{k,g} = [\text{Tr}(\bar{\mathbf{S}}_t \mathbf{M}_{k,g}^E \bar{\mathbf{S}}_{t'}^H \mathbf{J}_g)]_{t,t'=1}^T \in \mathbb{H}^T$ and $\bar{\mathcal{S}}_{k,g} = [\mathbf{M}_{k,g}^E \bar{\mathbf{S}}_1^H \mathbf{j}_g, \dots, \mathbf{M}_{k,g}^E \bar{\mathbf{S}}_T^H \mathbf{j}_g] \in \mathbb{C}^{MN \times T}$. Therefore, by applying Lemma 2, (C6) can be equivalently written as:

$$(\widetilde{\text{C6a}}): \begin{bmatrix} \hat{R}_{k,g}^{\text{th}} \sigma_g^2 \mathbf{I}_T + \mathcal{S}_{k,g} - \delta_{k,g}^{E_2} \mathbf{I}_T & \bar{\mathcal{S}}_{k,g}^H \\ \bar{\mathcal{S}}_{k,g} & \mathbf{M}_{k,g}^E - \frac{\delta_{k,g}^{E_2}}{(\varphi^{\text{tot}})^2} \mathbf{I}_{MN} \end{bmatrix} \succeq \mathbf{0}, \forall g, k,$$

$$(\widetilde{\text{C6b}}): \delta_{k,g}^{E_2} \geq 0, \forall g, k. \quad (48)$$

Thus, stage 1 of problem (43) can be written exploiting the auxiliary variables \mathbf{F}_k , \mathbf{F}_g , \mathbf{C}_k , and \mathbf{C}_g , as:

$$\begin{aligned} & \text{maximize} \quad \sum_{k \in \mathcal{K}} \log_2(\iota_k^N + \iota_k^D + \sigma_k^2) - \sum_{k \in \mathcal{K}} \log_2(\iota_k^D + \sigma_k^2) \\ & \mathbf{x}_{n,m}^{\text{Pin}}, \mathbf{F}_k, \mathbf{C}_k, \\ & \mathbf{F}_g^E, \mathbf{C}_g^E, \hat{\mathbf{H}}_k, \hat{\mathbf{h}}_k, \\ & \mathcal{H}_g, \mathbf{J}_g, \mathcal{J}_g, \mathcal{J}_g, \iota, \delta \end{aligned}$$

s.t. (C1), (C2), ($\widetilde{\text{C6a}}$), ($\widetilde{\text{C6b}}$), ($\widetilde{\text{C7a}}$), ($\widetilde{\text{C7b}}$), ($\widetilde{\text{C8a}}$), ($\widetilde{\text{C8b}}$), ($\widetilde{\text{C9a}}$) – ($\widetilde{\text{C9e}}$), ($\widetilde{\text{C10a}}$) – ($\widetilde{\text{C10e}}$),

$$(\widetilde{\text{C11}}): (x_{n,m}^{\text{Pin}} - x_k)^2 = \frac{1}{\text{Diag}(\mathbf{F}_k)_{l(n,m)}} - \hat{\beta}_{n,k}, \forall n, m, k,$$

$$(\widetilde{\text{C12}}): (x_{n,m}^{\text{Pin}} - x_{g,t}^E)^2 = \frac{1}{\text{Diag}(\mathbf{F}_g)_{l(n,m,t)}} - \hat{\beta}_{n,g,t}^E, \forall n, m, t, g,$$

$$(\widetilde{\text{C13}}): \text{Diag}(\mathbf{C}_k)_{l(n,m)} = \hat{\eta} \zeta_k^{n,m} (x_{n,m}^{\text{Pin}}), \forall n, m, k,$$

$$(\widetilde{\text{C14}}): \text{Diag}(\mathbf{C}_g)_{l(n,m,t)} = \hat{\eta} \zeta_{g,t}^{n,m} (x_{n,m}^{\text{Pin}}), \forall n, m, t, g, \quad (49)$$

where $\iota = \{\iota_k^N, \iota_k^D\}$, $\delta = \{\delta_k^D, \delta_k^N, \delta_{k,g}^{E_2}\}$, $\hat{\beta}_{n,k} = (y_k - D_n)^2 + d^2$, $\hat{\beta}_{n,g,t}^E = (y_{g,t} - D_n)^2 + d^2$, $\text{Diag}(\mathbf{F}_g)_{l(n,m,t)} = [\mathbf{F}_g]_{l(n,m,t), l(n,m,t)}$, $\text{Diag}(\mathbf{C}_g)_{l(n,m,t)} = [\mathbf{C}_g]_{l(n,m,t), l(n,m,t)}$, $l(n,m,t) = (t-1)MN + (n-1)M + m$, and $\text{Diag}(\mathbf{F}_k)_{l(n,m)} = [\mathbf{F}_k]_{l(n,m), l(n,m)}$, $\text{Diag}(\mathbf{C}_k)_{l(n,m)} = [\mathbf{C}_k]_{l(n,m), l(n,m)}$. The problem in (49) is nonconvex due to the equality constraints, the rank-one constraints, the bilinear couplings, and the DC format objective. We first handle the equalities and bilinear terms by replacing each equality with two inequalities and adopting the Frobenius norm to decouple matrix couplings [1], [15]. Taking ($\widetilde{\text{C9a}}$) as an example, it can be equivalent represented as:

$$\begin{aligned} (\widetilde{\text{C9aa}}): & \left\| \mathbf{F}_k + \hat{\mathbf{A}}_k^H \mathbf{C}_k \hat{\mathbf{A}}_k \right\|_F^2 - \left\| \mathbf{F}_k \right\|_F^2 - \left\| \hat{\mathbf{A}}_k^H \mathbf{C}_k \hat{\mathbf{A}}_k \right\|_F^2 - 2\text{Tr}(\mathbf{Y}_k \hat{\mathbf{H}}_k) \leq 0, \forall k, \\ (\widetilde{\text{C9ab}}): & 2\text{Tr}(\mathbf{Y}_k \hat{\mathbf{H}}_k) - \left\| \mathbf{F}_k + \hat{\mathbf{A}}_k^H \mathbf{C}_k \hat{\mathbf{A}}_k \right\|_F^2 + \left\| \mathbf{F}_k \right\|_F^2 + \left\| \hat{\mathbf{A}}_k^H \mathbf{C}_k \hat{\mathbf{A}}_k \right\|_F^2 \leq 0, \forall k, \end{aligned} \quad (50)$$

both of which remain non-convex but admit a DC structure. Similarly, the equality constraints ($\widetilde{\text{C11}}$), ($\widetilde{\text{C12}}$), ($\widetilde{\text{C13}}$), and ($\widetilde{\text{C14}}$) are represented as two inequality constraints labeled ‘‘a’’ and ‘‘b’’. Specifically, ($\widetilde{\text{C10a}}$) analogously follows the same structure, adopting the Frobenius-norm identity in (50). These transformations are omitted due to page limitations. Moreover, by directly applying Lemma 3, the rank-one constraints, ($\widetilde{\text{C9b}}$) – ($\widetilde{\text{C9d}}$) and ($\widetilde{\text{C10b}}$) – ($\widetilde{\text{C10d}}$), are also converted into their DC forms, identical in structure to (37).

However, the problem remains challenging due to the min-max nature of the constraints ($\widetilde{\text{C13a}}$)–($\widetilde{\text{C14b}}$). To address this, we take ($\widetilde{\text{C13a}}$) and ($\widetilde{\text{C13b}}$) as examples, which can be written as the logarithmic inequality:

$$\begin{aligned} (\widetilde{\text{C13a}}): & \bar{C}_k^{l(n,m)} + \log_2(1 + e^{-\vartheta \bar{\alpha}_k^{n,m}}) - \log_2(\hat{\eta}) \leq 0, \forall n, m, k, \\ (\widetilde{\text{C13b}}): & -\bar{C}_k^{l(n,m)} - \log_2(1 + e^{-\vartheta \bar{\alpha}_k^{n,m}}) + \log_2(\hat{\eta}) \leq 0, \forall n, m, k, \end{aligned} \quad (51)$$

where $\bar{C}_k^{l(n,m)} = \log_2(\text{Diag}(\mathbf{C}_k)_{l(n,m)})$ and $\bar{\alpha}_k^{n,m} = \frac{\min_{q \in \mathcal{Q}} \{d_{k,q}^{n,m}\}}{[\text{Diag}(\mathbf{F}_k)_{l(n,m)}]^{-1/2}}$. Noting that in ($\widetilde{\text{C13a}}$) and ($\widetilde{\text{C13b}}$) the term $+\log(1 + e^{\vartheta(\cdot)})$ is convex and strictly increasing, whereas $-\log(1 + e^{\vartheta(\cdot)})$ is concave and strictly decreasing, we intro-

duce the slack variables $\bar{\alpha}_{n,m,k}$ and $\bar{r}_{n,m,k}$ as:

$$\begin{aligned} (\widetilde{\text{C13c}}): \bar{\alpha}_{n,m,k} &\leq \frac{\mu_k^{n,m}(x_{n,m}^{\text{Pin}})}{[\text{Diag}(\mathbf{F}_k)_{l(n,m)}]^{-1/2}}, \forall n, m, k, \\ (\widetilde{\text{C13d}}): \bar{\alpha}_{n,m,k} &\geq \frac{\mu_k^{n,m}(x_{n,m}^{\text{Pin}})}{[\text{Diag}(\mathbf{F}_k)_{l(n,m)}]^{-1/2}}, \forall n, m, k, \\ (\widetilde{\text{C15a}}): [\text{Diag}(\mathbf{F}_k)_{l(n,m)}]^{-1/2} &\leq \bar{r}_{n,m,k}, \forall n, m, k, \\ (\widetilde{\text{C15b}}): [\text{Diag}(\mathbf{F}_k)_{l(n,m)}]^{-1/2} &\geq \bar{r}_{n,m,k}, \forall n, m, k. \end{aligned} \quad (52)$$

We then apply the triangle property, $\bar{r}_{n,m,k} \bar{\alpha}_{n,m,k} = \frac{1}{4} [(\bar{r}_{n,m,k} + \bar{\alpha}_{n,m,k})^2 - (\bar{r}_{n,m,k} - \bar{\alpha}_{n,m,k})^2]$, to decouple the two slack variables in constraints $(\widetilde{\text{C13a}})$ and $(\widetilde{\text{C13b}})$, as:

$$\begin{aligned} (\widetilde{\text{C13a}}): \log_2(\text{Diag}(\mathbf{C}_k)_{l(n,m)}) + \log_2(1 + e^{-\vartheta \bar{\alpha}_{n,m,k}}) - \log_2(\hat{\eta}) &\leq 0, \forall n, m, k, \\ (\widetilde{\text{C13b}}): -\log_2(\text{Diag}(\mathbf{C}_k)_{l(n,m)}) - \log_2(1 + e^{-\vartheta \bar{\alpha}_{n,m,k}}) + \log_2(\hat{\eta}) &\leq 0, \forall n, m, k, \\ (\widetilde{\text{C13c}}): \frac{(\bar{r}_{n,m,k} + \bar{\alpha}_{n,m,k})^2 - (\bar{r}_{n,m,k} - \bar{\alpha}_{n,m,k})^2}{4} - \mu_k^{n,m}(x_{n,m}^{\text{Pin}}) &\leq 0, \forall n, m, k, \\ (\widetilde{\text{C13d}}): \mu_k^{n,m}(x_{n,m}^{\text{Pin}}) - \frac{(\bar{r}_{n,m,k} + \bar{\alpha}_{n,m,k})^2 - (\bar{r}_{n,m,k} - \bar{\alpha}_{n,m,k})^2}{4} &\leq 0, \forall n, m, k. \end{aligned} \quad (53)$$

Here, $(\widetilde{\text{C13a}})$ and $(\widetilde{\text{C13b}})$ are in DC form, whereas the remaining difficulty lies in $\mu_k^{n,m}(x_{n,m}^{\text{Pin}})$ within $(\widetilde{\text{C13c}})$ – $(\widetilde{\text{C13d}})$. Following the same idea in (53), $(\widetilde{\text{C14a}})$ – $(\widetilde{\text{C14b}})$ can be equivalently transformed into $(\widetilde{\text{C14a}})$ – $(\widetilde{\text{C14d}})$ with the aid of $(\widetilde{\text{C16a}})$ – $(\widetilde{\text{C16b}})$ by introducing the slack variables $\bar{\alpha}_{n,m,g,t}^E$ and $\bar{r}_{n,m,g,t}^E$; details are omitted for brevity.

Nonetheless, the objective and constraints $(\widetilde{\text{C9aa}})$, $(\widetilde{\text{C9ab}})$, $(\widetilde{\text{C9b}})$ – $(\widetilde{\text{C9d}})$, $(\widetilde{\text{C10b}})$ – $(\widetilde{\text{C10d}})$, $(\widetilde{\text{C10aa}})$, $(\widetilde{\text{C10ab}})$, $(\widetilde{\text{C10b}})$, $(\widetilde{\text{C10c}})$, $(\widetilde{\text{C11a}})$, $(\widetilde{\text{C11b}})$, $(\widetilde{\text{C12a}})$, $(\widetilde{\text{C12b}})$, $(\widetilde{\text{C13a}})$ – $(\widetilde{\text{C13d}})$, and $(\widetilde{\text{C14a}})$ – $(\widetilde{\text{C14d}})$ exhibit a DC structure, which will be handled by adopting a MM algorithm. In addition, $(\widetilde{\text{C13c}})$, $(\widetilde{\text{C13d}})$, $(\widetilde{\text{C14c}})$, and $(\widetilde{\text{C14d}})$ involve min-max nonconvexity. Typically, we adopt Proposition 3 to obtain a performance lower bound for the objective at the $(i_2 + 1)$ -th iteration. With Proposition 5, the DC format rank-one constraints take the same structure as in (40) (details omitted to avoid repetition). Specifically, $(\widetilde{\text{C9b}}) - (\widetilde{\text{C9d}})$, $(\widetilde{\text{C10b}}) - (\widetilde{\text{C10d}}) \Rightarrow (\widetilde{\text{C9b}}) - (\widetilde{\text{C9d}})$, $(\widetilde{\text{C10b}}) - (\widetilde{\text{C10d}})$, respectively. Moreover, we derive global underestimation for the remaining nonconvex terms via first-order Taylor expansions:

$$\begin{aligned} (\widetilde{\text{C9aa}}): &\left\| \mathbf{F}_k + \hat{\mathbf{A}}_k^H \mathbf{C}_k \hat{\mathbf{A}}_k \right\|_F^2 - 2\text{Tr}(\mathbf{Y}_k \hat{\mathbf{H}}_k) + \left\| \hat{\mathbf{A}}_k^H \mathbf{C}_k^{(i_2)} \hat{\mathbf{A}}_k \right\|_F^2 + \left\| \mathbf{F}_k^{(i_2)} \right\|_F^2 \\ &- 2\text{Tr}(\hat{\mathbf{A}}_k \hat{\mathbf{A}}_k^H \mathbf{C}_k^{(i_2)} \hat{\mathbf{A}}_k \hat{\mathbf{A}}_k^H \mathbf{C}_k) - 2\text{Tr}(\mathbf{F}_k^{(i_2)H} \mathbf{F}_k) \leq 0, \forall k, \\ (\widetilde{\text{C9ab}}): &2\text{Tr}(\mathbf{Y}_k \hat{\mathbf{H}}_k) - 2\text{Tr}(\mathbf{F}_k^{(i_2)} + \hat{\mathbf{A}}_k^H \mathbf{C}_k^{(i_2)} \hat{\mathbf{A}}_k)^H (\mathbf{F}_k - \mathbf{F}_k^{(i_2)}) \\ &\left\| \hat{\mathbf{A}}_k^H \mathbf{C}_k \hat{\mathbf{A}}_k \right\|_F^2 - \left\| \mathbf{F}_k^{(i_2)} + \hat{\mathbf{A}}_k^H \mathbf{C}_k^{(i_2)} \hat{\mathbf{A}}_k \right\|_F^2 + \left\| \mathbf{F}_k \right\|_F^2 \\ &- 2\text{Tr}(\mathbf{F}_k^{(i_2)} + \hat{\mathbf{A}}_k^H \mathbf{C}_k^{(i_2)} \hat{\mathbf{A}}_k)^H \hat{\mathbf{A}}_k^H (\mathbf{C}_k - \mathbf{C}_k^{(i_2)}) \hat{\mathbf{A}}_k, \forall k, \\ (\widetilde{\text{C11a}}): &(x_{n,m}^{\text{Pin}} - x_k)^2 - \frac{1}{z_{n,m,k}^{(i_2)}} + \frac{(z_{n,m,k} - z_{n,m,k}^{(i_2)})}{(z_{n,m,k}^{(i_2)})^2} + \hat{\beta}_{n,k} \leq 0, \forall n, m, k, \\ (\widetilde{\text{C11b}}): &\frac{1}{z_{n,m,k}} - \hat{\beta}_{n,k} - \left(x_{n,m}^{\text{Pin}(i_2)} - x_k \right)^2 \\ &- 2 \left(x_{n,m}^{\text{Pin}(i_2)} - x_k \right) \left(x_{n,m}^{\text{Pin}} - x_{n,m}^{\text{Pin}(i_2)} \right) \leq 0, \forall n, m, k, \end{aligned}$$

$$\begin{aligned} (\widetilde{\text{C13a}}): &\log_2(\text{Diag}(\mathbf{C}_k)_{l(n,m)}) + \frac{(\text{Diag}(\mathbf{C}_k)_{l(n,m)} - \text{Diag}(\mathbf{C}_k^{(i_2)})_{l(n,m)})}{\text{Diag}(\mathbf{C}_k^{(i_2)})_{l(n,m)}} \\ &+ \log_2(1 + \exp[-\vartheta \bar{\alpha}_{n,m,k}]) - \log_2(\hat{\eta}) \leq 0, \forall n, m, k, \\ (\widetilde{\text{C13b}}): &-\log_2(\text{Diag}(\mathbf{C}_k)_{l(n,m)}) - \log_2(1 + \exp[-\vartheta \bar{\alpha}_{n,m,k}]) \\ &+ \log_2(\hat{\eta}) + \frac{\vartheta e^{-\vartheta \bar{\alpha}_{n,m,k}} (\bar{\alpha}_{n,m,k} - \bar{\alpha}_{n,m,k}^{(i_2)})}{1 + \exp[-\vartheta \bar{\alpha}_{n,m,k}]} \leq 0, \forall n, m, k, \\ (\widetilde{\text{C15a}}): &z_{n,m,k}^{-1} - \left(\bar{r}_{n,m,k}^{(i_2)} \right)^2 + 2\bar{r}_{n,m,k}^{(i_2)} (\bar{r}_{n,m,k} - \bar{r}_{n,m,k}^{(i_2)}) \leq 0, \forall n, m, k, \\ (\widetilde{\text{C15b}}): &\bar{r}_{n,m,k}^2 - \left(\frac{1}{z_{n,m,k}^{(i_2)}} - \frac{(z_{n,m,k} - z_{n,m,k}^{(i_2)})}{(z_{n,m,k}^{(i_2)})^2} \right) \leq 0, \forall n, m, k, \end{aligned} \quad (54)$$

where $\text{Diag}(\mathbf{F}_k)_{l(n,m)} = z_{n,m,k}$ and $\text{Diag}(\mathbf{F}_g^E)_{l(n,m,t)} = z_{n,m,g,t}^E$ for notational simplicity. The terms “ (i_2) ” are the solutions obtained at iteration i_2 for the corresponding variables. Also, constraints $(\widetilde{\text{C10aa}})$, $(\widetilde{\text{C10ab}})$, $(\widetilde{\text{C12a}})$, $(\widetilde{\text{C12b}})$, $(\widetilde{\text{C14a}})$, $(\widetilde{\text{C14b}})$, $(\widetilde{\text{C16a}})$, and $(\widetilde{\text{C16b}})$ are omitted to avoid repetition, as they are analogous to $(\widetilde{\text{C9aa}})$, $(\widetilde{\text{C9ab}})$, $(\widetilde{\text{C11a}})$, $(\widetilde{\text{C11b}})$, $(\widetilde{\text{C13a}})$, $(\widetilde{\text{C13b}})$, $(\widetilde{\text{C15a}})$, and $(\widetilde{\text{C15b}})$, respectively.

To handle the sigmoid-involved constraints, we take $(\widetilde{\text{C13c}})$ and $(\widetilde{\text{C13d}})$ as examples. We first map the LoS availability metric $d_{k,q}^{m,m}$ of PA m on waveguide n for user u_k with respect to block q into a one-dimensional affine form as $d_{k,q}^{m,m} = \max_{i \in \mathcal{I}_{k,q}} \{ [\mathbf{a}_{k,q}^i]_1 x_{n,m}^{\text{Pin}} + \bar{b}_{k,q}^i \}$, where $\bar{b}_{k,q}^i = [\mathbf{a}_{k,q}^i]_2 y_n^{\text{FP}} + [\mathbf{a}_{k,q}^i]_3 d - b_{k,q}^i$ is a constant. Inspired by [11], we then identify, for each blockage q , the most active plane contributing to $d_{k,q}^{m,m}$ at the current PA position $x_{n,m}^{\text{Pin}(i_2)}$ in the i_2 -th iteration, i.e., $i^*(q) \in \arg \max_{i \in \mathcal{I}_{k,q}} \{ [\mathbf{a}_{k,q}^i]_1 x_{n,m}^{\text{Pin}(i_2)} + \bar{b}_{k,q}^i \}$, $\forall n, m, k, q$. Given these active planes $i^*(q)$, $\forall q$, we substitute them into $\mu_k^{n,m}(x_{n,m}^{\text{Pin}})$ and, at the $(i_2 + 1)$ -th iteration of the MM algorithm, construct a concave lower bound of $\mu_k^{n,m}(x_{n,m}^{\text{Pin}})$ via a first-order Taylor expansion around $x_{n,m}^{\text{Pin}(i_2)}$, namely:

$$\begin{aligned} \mu_k^{n,m}(x_{n,m}^{\text{Pin}}) &\geq \mu_{k,\text{LB}}^{n,m(i_2)}(x_{n,m}^{\text{Pin}}) \\ &\triangleq \min_{q \in \mathcal{Q}} \left\{ d_{k,q}^{n,m}(x_{n,m}^{\text{Pin}(i_2)}) + [\mathbf{a}_{k,q}^{i^*}]_1 (x_{n,m}^{\text{Pin}} - x_{n,m}^{\text{Pin}(i_2)}) \right\}, \forall n, m, k. \end{aligned} \quad (55)$$

Therefore, a convex subset of $(\widetilde{\text{C13c}})$ of the $(i_2 + 1)$ -th iteration MM can be written as:

$$\begin{aligned} (\widetilde{\text{C13c}}): &\frac{(\bar{r}_{n,m,k} + \bar{\alpha}_{n,m,k})^2 - (\bar{r}_{n,m,k} - \bar{\alpha}_{n,m,k})^2}{4} - \mu_{k,\text{LB}}^{n,m(i_2)}(x_{n,m}^{\text{Pin}}) \\ &+ \frac{(\bar{r}_{n,m,k}^{(i_2)} - \bar{\alpha}_{n,m,k}^{(i_2)}) (\bar{\alpha}_{n,m,k} - \bar{\alpha}_{n,m,k}^{(i_2)}) - (\bar{r}_{n,m,k} - \bar{r}_{n,m,k}^{(i_2)})}{2} \leq 0, \forall n, m, k, \end{aligned} \quad (56)$$

where $(\widetilde{\text{C13c}}) \Rightarrow (\widetilde{\text{C13c}})$. Similarly, to construct a convex upper bound for $\mu_k^{n,m}(x_{n,m}^{\text{Pin}})$, we identify, for each PA–user pair, the most critical blockage at the current iterate $x_{n,m}^{\text{Pin}(i_2)}$ as $q^*(i) \in \arg \min_{q \in \mathcal{Q}} \{ d_{k,q}^{n,m}(x_{n,m}^{\text{Pin}(i_2)}) \}$, $\forall n, m, k, i$. Using this active blockage index $q^*(i)$, we then establish a convex upper bound of $\mu_k^{n,m}(x_{n,m}^{\text{Pin}})$ and hence obtain a convex inner approximation of constraint $(\widetilde{\text{C13d}})$ at the $(i_2 + 1)$ -th MM iteration via a first-order Taylor expansion as:

$$\mu_k^{n,m}(x_{n,m}^{\text{Pin}}) \leq \mu_{k,\text{UB}}^{n,m}(x_{n,m}^{\text{Pin}}) = \max_{i \in \mathcal{I}_{k,q^*}} \{ [\mathbf{a}_{k,q^*}^i]_1 (x_{n,m}^{\text{Pin}}) + \bar{b}_{k,q^*}^i \}, \forall n, m, k,$$

$$\begin{aligned} \text{(C13d)}: \mu_{k,UB}^{n,m}(x_{n,m}^{\text{Pin}}) + \frac{(\bar{r}_{n,m,k} - \bar{\alpha}_{n,m,k})^2 - (\bar{r}_{n,m,k}^{(i_2)} + \bar{\alpha}_{n,m,k}^{(i_2)})^2}{4} \\ - \frac{(\bar{r}_{n,m,k}^{(i_2)} + \bar{\alpha}_{n,m,k}^{(i_2)})(\bar{\alpha}_{n,m,k} - \bar{\alpha}_{n,m,k}^{(i_2)}) + (\bar{r}_{n,m,k} - \bar{r}_{n,m,k}^{(i_2)})}{2} \leq 0, \forall n, m, k, \end{aligned} \quad (57)$$

Respectively. Note that we omit the details for $\widetilde{\text{(C14c)}}$ and $\widetilde{\text{(C14d)}}$, as they are analogous to $\widetilde{\text{(C13c)}}$ and $\widetilde{\text{(C13d)}}$ in (56) and (57), respectively.

Accordingly, the $(i_2 + 1)$ -th MM iteration for stage 1 of PA positioning is as follows:

$$\begin{aligned} & \underset{\substack{\mathbf{x}_{n,m}^{\text{Pin}}, \mathbf{f}_k, \mathbf{c}_k, \ell \\ \mathbf{F}_g^E, \mathbf{C}_g^E, \hat{\mathbf{h}}_k, \hat{\mathbf{h}}_k, \\ \mathbf{J}_g, \mathbf{j}_g, \mathcal{J}_g, \mathcal{H}_k, \delta}}{\text{maximize}} \sum_{k \in \mathcal{K}} \log_2(\ell_k^N + \ell_k^D + \sigma_k^2) + \bar{R}(\ell_k^{D(i_2)}) \\ \text{s.t. } & \text{(C1), (C2), } \widetilde{\text{(C6a)}}, \widetilde{\text{(C6b)}}, \widetilde{\text{(C7a)}}, \widetilde{\text{(C7b)}}, \widetilde{\text{(C8a)}}, \widetilde{\text{(C8b)}}, \widetilde{\text{(C9aa)}}, \\ & \widetilde{\text{(C9ab)}}, \widetilde{\text{(C9b)}} - \widetilde{\text{(C9d)}}, \widetilde{\text{(C10aa)}}, \widetilde{\text{(C10ab)}}, \widetilde{\text{(C10b)}} - \widetilde{\text{(C10d)}}, \\ & \widetilde{\text{(C11a)}}, \widetilde{\text{(C11b)}}, \widetilde{\text{(C12a)}}, \widetilde{\text{(C12b)}}, \widetilde{\text{(C13a)}} - \widetilde{\text{(C13d)}}, \\ & \widetilde{\text{(C14a)}} - \widetilde{\text{(C14d)}}, \widetilde{\text{(C15a)}}, \widetilde{\text{(C15b)}}, \widetilde{\text{(C16a)}}, \widetilde{\text{(C16b)}}, \end{aligned} \quad (58)$$

where $\bar{\alpha} = \{\bar{\alpha}_{n,m,k}, \bar{\alpha}_{n,m,g,t}^E\}$ and $\bar{r} = \{\bar{r}_{n,m,k}, \bar{r}_{n,m,g,t}^E\}$ for simplifying the notations. The resulting problem in (58) is convex and can be directly solved using CVX.

B. Phase Shift-based Small Scale Movement

With the coarse PA positions fixed, we next refine the phase shifts induced by PA displacements, i.e., we optimize $\mathbf{a}_k, \mathbf{a}_g^E, \mathbf{x}^{\text{Pin}}$ given $\mathbf{f}_k, \mathbf{f}_g^E, \mathbf{c}_k, \mathbf{c}_g^E$. Define $\hat{\chi}_k = \mathbf{f}_k \odot \mathbf{c}_k$, such $\hat{\mathbf{h}}_k = \mathbf{A}_k^D \hat{\chi}_k$, where $\mathbf{A}_k^D = \text{diag}(\mathbf{a}_k)$ is diagonal with unit-modulus entries. Then:

$$\mathbf{h}_k = \mathbf{A}_k^D (\hat{\chi}_k + \Delta \chi_k), \|\Delta \mathbf{h}_k\|_2 \leq \wp_k \Leftrightarrow \|\Delta \chi_k\|_2 \leq \wp_k, \forall k. \quad (59)$$

Recalling (C7) and (C8) in (44) and exploiting the transformation in (59), we lift the phase-shift variables as $\mathbf{A}_k = \mathbf{a}_k \mathbf{a}_k^H$, $\forall k$, and $\mathbf{A}_g^E = \mathbf{a}_g^E (\mathbf{a}_g^E)^H$, $\forall g$. Noting that $\mathbf{A}_k^{DH} \mathbf{Y}_k \mathbf{A}_k^D = \mathbf{A}_k^T \odot \mathbf{Y}_k$, the resulting performance lower bound and the associated constraints (C7) and (C8), after applying Lemma 1, can be written in terms of $\mathbf{A}_k, \mathbf{A}_g^E$ as:

$$\begin{aligned} & \sum_{k \in \mathcal{K}} \log_2(\ell_k^N + \ell_k^D + \sigma_k^2) - \sum_{k \in \mathcal{K}} \log_2(\ell_k^D + \sigma_k^2) \quad \text{s.t.} \\ \text{(C7a)}: & \begin{bmatrix} \mathbf{A}_k^Y - \delta_k^N \mathbf{I}_{MN} & \mathbf{A}_k^Y \hat{\chi}_k \\ \mathbf{A}_k^Y \hat{\chi}_k^H & \hat{\chi}_k^H \mathbf{A}_k^Y \hat{\chi}_k - \ell_k^N + \delta_k^N \wp_k^2 \end{bmatrix} \succeq \mathbf{0}, \forall k, \\ \text{(C7b)}: & \delta_k^N \geq 0, \forall k, \quad \text{(C8b)}: \delta_k^D \geq 0, \forall k, \\ \text{(C8a)}: & \begin{bmatrix} \delta_k^D \mathbf{I}_{MN} - \mathbf{A}_k^Z & -\mathbf{A}_k^Z \hat{\chi}_k \\ -(\mathbf{A}_k^Z \hat{\chi}_k)^H & \ell_k^D - \hat{\chi}_k^H \mathbf{A}_k^Z \hat{\chi}_k - \delta_k^D \wp_k^2 \end{bmatrix} \succeq \mathbf{0}, \forall k, \\ \text{(C9a)}: & \text{Rank}(\mathbf{A}_k) = 1, \forall k, \quad \text{(C9b)}: \mathbf{A}_k \succeq \mathbf{0}, \text{diag}(\mathbf{A}_k) = \mathbf{1}, \forall k, \end{aligned} \quad (60)$$

where $\mathbf{A}_k^Y = \mathbf{A}_k^T \odot \mathbf{Y}_k$ and $\mathbf{A}_k^Z = \mathbf{A}_k^T \odot \bar{\mathbf{Z}}_k$.

We then recall $\widetilde{\text{(C6)}}$ in (44) and, following the same idea as in (60), define $\hat{\chi}_{g,t}^E = \mathbf{f}_{g,t}^E \odot \mathbf{c}_{g,t}^E$ and $\mathbf{A}_{E_{g,t}}^D = \text{diag}(\mathbf{a}_{g,t}^E) \in \mathbb{C}^{MN \times MN}$, $\forall g, t$, so that the nominal EA channel can be written as $\hat{\mathbf{H}}_{E_g} = [\mathbf{A}_{E_{g,1}}^D \hat{\chi}_{g,1}^E, \dots, \mathbf{A}_{E_{g,T}}^D \hat{\chi}_{g,T}^E] \in \mathbb{C}^{MN \times T}$. The deterministic and uncertain parts are collected as $\hat{\mathbf{X}}_{E_g} = [\hat{\chi}_{g,1}^E, \dots, \hat{\chi}_{g,T}^E]$ and $\Delta \mathbf{X}_{E_g} =$

$[\Delta \chi_{g,1}^E, \dots, \Delta \chi_{g,T}^E] \in \mathbb{C}^{MN \times T}$, respectively. We further define the known matrix $\hat{\mathbf{X}}_{E_g}^D = \text{blkdiag}(\hat{\chi}_{g,1}^E, \dots, \hat{\chi}_{g,T}^E)$ and $\Delta \mathbf{X}_{E_g}^D = \text{blkdiag}(\Delta \chi_{g,1}^E, \dots, \Delta \chi_{g,T}^E) \in \mathbb{C}^{MNT \times T}$, we have $\|\Delta \mathbf{H}_{E_g}\|_F \leq \wp_g^{\text{tot}} \Leftrightarrow \|\Delta \mathbf{X}_{E_g}\| \leq \wp_g^{\text{tot}}$. With $\mathbf{A}_g^E = \mathbf{a}_g^E (\mathbf{a}_g^E)^H$ and $\tilde{\mathbf{M}}_{k,g}^E = (\mathbf{1}_T \mathbf{1}_T^T) \otimes \mathbf{M}_{k,g}^E \in \mathbb{C}^{MNT \times MNT}$, the LMIs associated with the EA constraints, after applying Lemma 2, can be written as:

$$\text{(C6a)}: \begin{bmatrix} (\hat{\mathbf{X}}_{E_g}^D)^H \mathbf{A}_{k,g}^M \hat{\mathbf{X}}_{E_g}^D + (\hat{r}_{k,g}^{\text{th}} \sigma_g^2 - \delta_{k,g}^{E_3}) \mathbf{I}_T & (\mathbf{A}_{k,g}^M \hat{\mathbf{X}}_{E_g}^D)^H \\ \mathbf{A}_{k,g}^M \hat{\mathbf{X}}_{E_g}^D & \mathbf{A}_{k,g}^M + \frac{\delta_{k,g}^{E_3}}{(\wp_g^{\text{tot}})^2} \mathbf{I}_{MNT} \end{bmatrix} \succeq \mathbf{0}, \forall g, k,$$

$$\text{(C6b)}: \delta_{k,g}^{E_3} \geq 0, \forall g, \quad \text{(C10a)}: \text{Rank}(\mathbf{A}_g^E) = 1, \forall g,$$

$$\text{(C10b)}: \mathbf{A}_g^E \succeq \mathbf{0}, \quad \text{diag}(\mathbf{A}_g^E) = \mathbf{1}_{MNT}, \forall g, \quad (61)$$

where $\mathbf{A}_{k,g}^M = (\mathbf{A}_g^E)^T \odot \tilde{\mathbf{M}}_{k,g}^E$. Thus, the second phase of the PA positioning problem, with variables \mathbf{A}_k and \mathbf{A}_g to characterize the pure phase-alignment components for legitimate user k and EA g , respectively, can be formulated as:

$$\begin{aligned} & \underset{\substack{\mathbf{x}_{n,m}^{\text{Pin}}, \mathbf{A}_k, \ell, \delta, \\ \mathbf{A}_g^E, \delta, \theta_{l(n,m),k}, \theta_{l(n,m,t),g}}}{\text{maximize}} \sum_{k \in \mathcal{K}} \log_2(\ell_k^N + \ell_k^D + \sigma_k^2) - \sum_{k \in \mathcal{K}} \log_2(\ell_k^D + \sigma_k^2) \\ \text{s.t. } & \text{(C1), (C2), } \widetilde{\text{(C6a)}}, \widetilde{\text{(C6b)}}, \widetilde{\text{(C7a)}}, \widetilde{\text{(C7b)}}, \widetilde{\text{(C8a)}}, \\ & \widetilde{\text{(C8b)}}, \widetilde{\text{(C9a)}}, \widetilde{\text{(C9b)}}, \widetilde{\text{(C10a)}}, \widetilde{\text{(C10b)}}, \\ \text{(C11)}: & \theta_{l(n,m),k} = \frac{2\pi \sqrt{(x_{n,m}^{\text{Pin}} - x_k)^2 + \beta_{n,k}}}{\lambda} + \frac{2\pi x_{n,m}^{\text{Pin}}}{\lambda}, \forall n, m, k, \\ \text{(C12)}: & [\mathbf{A}_k]_{l(n,m),l(n',m')} = e^{-j(\theta_{l(n,m),k} - \theta_{l(n',m'),k})}, \forall n, m, n', m', k, \\ \text{(C13)}: & \theta_{l(n,m,t),g}^E = \frac{2\pi \sqrt{(x_{n,m}^{\text{Pin}} - x_{g,t}^E)^2 + \beta_{n,g,t}^E}}{\lambda} + \frac{2\pi x_{n,m}^{\text{Pin}}}{\lambda}, \forall n, m, t, g, \\ \text{(C14)}: & [\mathbf{A}_g^E]_{l(n,m,t),l(n',m',t')} = e^{-j(\theta_{l(n,m,t),g}^E - \theta_{l(n',m',t'),g}^E)}, \forall n, m, t, n', m', t', g. \end{aligned} \quad (62)$$

Noting the multiple nonconvex equality constraints in (62), we handle them via the procedure in (50): $\widetilde{\text{(C11a)}}$ and $\widetilde{\text{(C11b)}}$ replace the equality in $\widetilde{\text{(C11)}}$ with “ \leq ” and “ \geq ,” respectively, and $\widetilde{\text{(C13a)}}$ and $\widetilde{\text{(C13b)}}$ do the same for $\widetilde{\text{(C13)}}$. Moreover, since $\text{Rank}(\mathbf{A}_k) = 1$, $\mathbf{A}_k \succeq \mathbf{0}$, $\forall k$, and $\text{Rank}(\mathbf{A}_g) = 1$, $\mathbf{A}_g \succeq \mathbf{0}$, $\forall g$, matrices \mathbf{A}_k and \mathbf{A}_g^E are fully characterized by any nonzero column. Without loss of generality, we adopt their first columns to simplify notation [1]. By trigonometric identities, $\widetilde{\text{(C12)}}$ can be equivalently transformed into:

$$\text{(C12a)}: \Re([\mathbf{A}_k]_{i,1}) = \cos(\hat{\theta}_{i,k}), \forall i \in \{2, \dots, MN\},$$

$$\text{(C12b)}: \Im([\mathbf{A}_k]_{i,1}) = -\sin(\hat{\theta}_{i,k}), \forall i \in \{2, \dots, MN\}, \quad (63)$$

where $\hat{\theta}_{i,k} = \theta_{i,k} - \theta_{1,k}$ and index i maps to the pair (n, m) through $i = (n-1)M + m$, and $\hat{\theta}_{i,g}^E = \theta_{i,g}^E - \theta_{1,g}^E$ with $\bar{i} = (t-1)MN + (n-1)M + m$. Note that $\widetilde{\text{(C14a)}}$ and $\widetilde{\text{(C14b)}}$ analogy to (63), thus their details are omitted.

Currently, nonconvexity arises from $\widetilde{\text{(C9a)}}$, $\widetilde{\text{(C10a)}}$, $\widetilde{\text{(C11a)}}$, $\widetilde{\text{(C13a)}}$, and the objective due to their DC form. More challengingly, $\widetilde{\text{(C12a)}}$, $\widetilde{\text{(C12b)}}$, $\widetilde{\text{(C14a)}}$, and $\widetilde{\text{(C14b)}}$ suffer from periodicity. We adopt Proposition 3 to handle the objective's nonconvex terms and Proposition 5 to handle

Algorithm 1 Overall BCD Algorithm

- 1: **Initialize:** Set the maximum number of iterations τ_{\max} and the convergence tolerance $\tau_{\text{tol}} \rightarrow 0$. Initialize the iteration index $\tau = 0$ and the optimization variables $\mathbf{W}_k^{(\tau)}, \forall k, \mathbf{V}^{(\tau)}, \mathbf{P}^{(\tau)}$, and $\mathbf{x}^{\text{Pin}(\tau)}$.
 - 2: **repeat** ▷ Main Loop: BCD
 - 3: **Subproblem 1:** For fixed $\mathbf{x}^{\text{Pin}(\tau)}$, solve the problem in (42) to obtain $\{\mathbf{W}_k^{(\tau+1)}, \mathbf{V}^{(\tau+1)}, \mathbf{P}^{(\tau+1)}\}$.
 - 4: **Subproblem 2:** With $\{\mathbf{W}_k^{(\tau+1)}, \mathbf{V}^{(\tau+1)}, \mathbf{P}^{(\tau+1)}\}$, solve the following 2 stages:
 - 5: *Stage 1:* Solving problem in (58) to obtain a coarse solution $\mathbf{x}_c^{\text{Pin}(\tau+1)}$.
 - 6: *Stage 2:* Starting from $\mathbf{x}_c^{\text{Pin}(\tau+1)}$, solve the phase-refinement PA in (66) to obtain $\mathbf{x}^{\text{Pin}(\tau+1)}$.
 - 7: Update $\tau \leftarrow \tau + 1$.
 - 8: **until** $\tau = \tau_{\max}$ or performance gap $\leq \tau_{\text{tol}}$.
 - 9: **return** $\{\mathbf{W}_k^*, \forall k, \mathbf{V}^*, \mathbf{P}^*, \mathbf{x}^{\text{Pin}^*}\} = \{\mathbf{W}_k^{(\tau)}, \forall k, \mathbf{V}^{(\tau)}, \mathbf{P}^{(\tau)}, \mathbf{x}^{\text{Pin}(\tau)}\}$.
-

the rank-one DC constraints, deriving convex subsets with $(\widehat{\text{C9a}}) \Rightarrow (\widehat{\text{C9a}})$ and $(\widehat{\text{C10a}}) \Rightarrow (\widehat{\text{C10a}})$. Moreover, the convex subset of $(\widehat{\text{C10a}})$ obtained via first-order Taylor expansion is:

$$\begin{aligned}
 (\widehat{\text{C11a}}): & \theta_{l(n,m),k} - \left(\frac{2\pi(x_{n,m}^{\text{Pin}(i_3)} - x_k)}{\lambda \sqrt{(x_{n,m}^{\text{Pin}(i_3)} - x_k)^2 + \hat{\beta}_{n,k}}} + \frac{2\pi}{\lambda} \right) (x_{n,m}^{\text{Pin}} - x_{n,m}^{\text{Pin}(i_3)}) \\
 & - \frac{2\pi \sqrt{(x_{n,m}^{\text{Pin}(i_3)} - x_k)^2 + \hat{\beta}_{n,k}}}{\lambda} - \frac{2\pi x_{n,m}^{\text{Pin}(i_3)}}{\lambda} \leq 0, \forall n, m, k, \quad (64)
 \end{aligned}$$

where details of $(\widehat{\text{C13a}})$ are omitted as it is analogous to $(\widehat{\text{C11a}})$, $(\widehat{\text{C11a}}) \Rightarrow (\widehat{\text{C11a}})$ and $(\widehat{\text{C13a}}) \Rightarrow (\widehat{\text{C13a}})$. The terms with “ (i_3) ” are the solutions of the i_3 -th iteration for the respective variables. To further address the intrinsic nonconvexity, we introduce a penalty-based MM algorithm [45], [46]. We let $\Gamma([\mathbf{A}_k]_{i,1}, \hat{\theta}_{i,k}) = |\Re([\mathbf{A}_k]_{i,1}) - \cos(\hat{\theta}_{i,k})|^2 + |\Im([\mathbf{A}_k]_{i,1}) + \sin(\hat{\theta}_{i,k})|^2$ and $\Gamma([\mathbf{A}_g^E]_{i,1}, \hat{\theta}_{i,g}^E) = |\Re([\mathbf{A}_g^E]_{i,1}) - \cos(\hat{\theta}_{i,g}^E)|^2 + |\Im([\mathbf{A}_g^E]_{i,1}) + \sin(\hat{\theta}_{i,g}^E)|^2$. The $\rho_1, \rho_2 > 0$ are penalty coefficients imposing costs on violations of $(\widehat{\text{C12a}})$, $(\widehat{\text{C12b}})$, and $(\widehat{\text{C14a}})$, $(\widehat{\text{C14b}})$. Specifically, the penalty formulation is equivalent to the original problem, when ρ_1 and ρ_2 are sufficient large, i.e., $\rho_1, \rho_2 \rightarrow \infty$ [45], [46]. We then apply MM with a Lipschitz-gradient surrogate to establish a global upper bound [47] for $\Gamma([\mathbf{A}_k]_{i,1}, \hat{\theta}_{i,k})$:

$$\begin{aligned}
 \overline{\Phi}_{i,k}^{(i_3)} = & 2(\hat{\Re}_{i,k}^{(i_3)} \sin \hat{\theta}_{i,k}^{(i_3)} + \hat{\Im}_{i,k}^{(i_3)} \cos \hat{\theta}_{i,k}^{(i_3)}) \Delta \hat{\theta}_{i,k} + 2\hat{\Re}_{i,k}^{(i_3)} \Delta \Re_{i,k} + 2\hat{\Im}_{i,k}^{(i_3)} \Delta \Im_{i,k} \\
 & + \frac{L_{\text{AR}}}{2} \Delta \Re_{i,k} + \frac{L_{\text{AI}}}{2} \Delta \Im_{i,k} + \frac{L_{\text{TH}}}{2} (\Delta \hat{\theta}_{i,k})^2 + \Phi^{(i_3)}, \forall i, k, \quad (65)
 \end{aligned}$$

where $\hat{\Re}_{i,k}^{(i_3)} = \Re([\mathbf{A}_k]_{i,1}^{(i_3)}) - \cos \hat{\theta}_{i,k}^{(i_3)}$, $\hat{\Im}_{i,k}^{(i_3)} = \Im([\mathbf{A}_k]_{i,1}^{(i_3)}) + \sin \hat{\theta}_{i,k}^{(i_3)}$, $\Delta \hat{\theta}_{i,k} = \hat{\theta}_{i,k} - \hat{\theta}_{i,k}^{(i_3)}$, $\Delta \Re_{i,k} = \Re([\mathbf{A}_k]_{i,1}) - \Re([\mathbf{A}_k]_{i,1}^{(i_3)})$, $\Delta \Im_{i,k} = \Im([\mathbf{A}_k]_{i,1}) - \Im([\mathbf{A}_k]_{i,1}^{(i_3)})$. Note that the global upper bound for $\Gamma([\mathbf{A}_g^E]_{i,1}, \hat{\theta}_{i,g}^E)$ is denoted by $\overline{\Gamma}_{i,g}^{(i_3)}$ and follows the same structure as (65); details are omitted due to page limits. The Lipschitz constants are $L_{\text{AR}} = L_{\text{AI}} = 2, L_{\text{TH}} = 4$, obtained

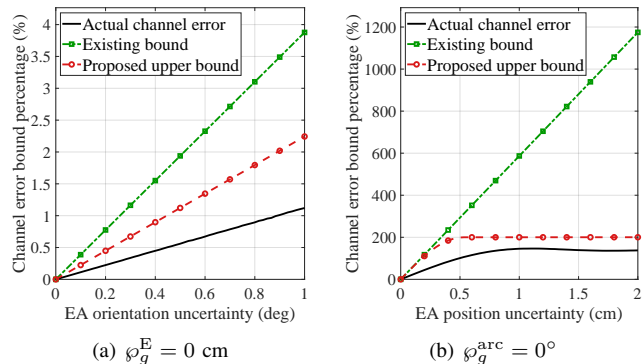


Fig. 5. Proposed channel error bound when $N = 5, M = 2$, and $T = 2$.

from the maximum curvature [47]. Accordingly, the $(i_3 + 1)$ -th iteration of the penalty-based MM method for stage 2 of the PA positioning problem can be expressed as:

$$\begin{aligned}
 & \underset{\mathbf{x}_n^{\text{Pin}}, \mathbf{A}_k, \ell, \delta, \mathbf{A}_g^E, k \in \mathcal{K}}{\text{maximize}} \quad \sum_{k \in \mathcal{K}} \log_2 (l_k^N + l_k^D + \sigma_k^2) + \bar{R}(l_k^{D(i_3)}) \\
 & \hat{\theta}_{i,k}, \hat{\theta}_{i,g}^E, \theta_{l(n,m),k}, \theta_{l(n,m,t),g} \\
 & - \rho_1 \sum_{k=1}^K \sum_{i=2}^{MN} \hat{\Gamma}_{i,k}^{(i_3)} - \rho_2 \sum_{g=1}^G \sum_{\bar{i}=2}^{MNT} \bar{\Gamma}_{\bar{i},g}^{(i_3)} \\
 & \text{s.t. (C1), (C2), } (\widehat{\text{C6a}}), (\widehat{\text{C6b}}), (\widehat{\text{C7a}}), (\widehat{\text{C7b}}), (\widehat{\text{C8a}}), \\
 & (\widehat{\text{C8b}}), (\widehat{\text{C9a}}), (\widehat{\text{C9b}}), (\widehat{\text{C10a}}), (\widehat{\text{C10b}}), (\widehat{\text{C11a}}), \\
 & (\widehat{\text{C11b}}), (\widehat{\text{C13a}}), \text{ and } (\widehat{\text{C13b}}). \quad (66)
 \end{aligned}$$

where the resulting problem in (66) is convex and can be directly solved adopting standard convex optimization solvers. This yields a suboptimal solution to the problem.

At each iteration of the BCD algorithm, one block of optimization variables is optimized until convergence to a predefined tolerance, while other blocks remain fixed. We summarize the proposed BCD-based algorithm in **Algorithm 1**, which is guaranteed to converge to a suboptimal solution of (20) within polynomial-time computational complexity [15], [24].

VI. SIMULATION RESULTS

This section evaluates the performance of the proposed multi-waveguide, multi-PA-assisted secure and robust system at the carrier frequency $f_c = 28$ GHz via numerical simulations. Unless otherwise stated, all results are averaged over multiple random realizations of user locations within a $15 \text{ m} \times 15 \text{ m}$ area, based on the configuration depicted in Fig. 1. We set the smoothing parameter, number of blockages, and waveguide height to $\vartheta = 500, Q = 2, d = 5 \text{ m}$, respectively, and fix the threshold of achievable rate for EA to $R_{\text{th}} = 1$ bits/s/Hz. The dielectric waveguides are fabricated from polytetrafluoroethylene (PTFE) [36] with parameters: $\eta_{\text{eff}} = 1.42, \epsilon_r = 2.1$, and $\tan(\delta_e) = 2 \times 10^{-4}$. The blockages are randomly generated in each realization: their length along the y -coordinate is fixed at 2.8 m , while their x -coordinate and height are drawn randomly from $[3, 5] \text{ m}$ and $[5, 8] \text{ m}$, respectively. To quantify the channel-estimation uncertainty, we define the maximum normalized estimation error of the legitimate channels as $\kappa_k = \varphi_k / \|\mathbf{h}_k\|_2$ and set $\kappa_k = \kappa, \forall k$,

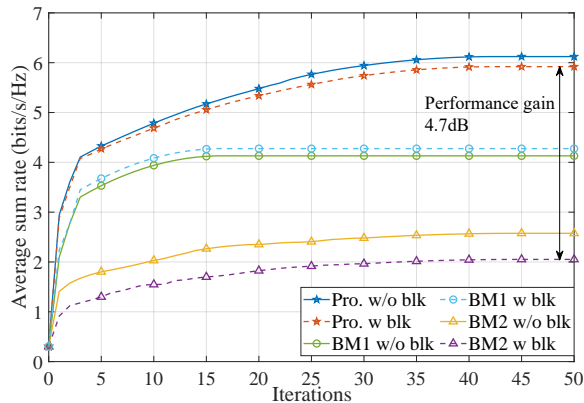
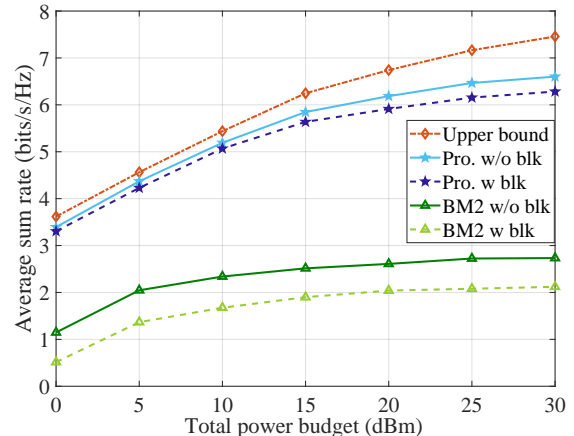


Fig. 6. Convergence of the proposed algorithm against multiple benchmarks under different system settings with $K = 2$, $G = 1$, $T = 2$, $P_{\max} = 20$ dBm, $\kappa^2 = 0.1$, $\phi_g^{\text{arc}} = 1^\circ$, $\phi_g^{\text{E}} = 1$ cm, and $R_{\text{tol}} = 1$ bits/s/Hz.

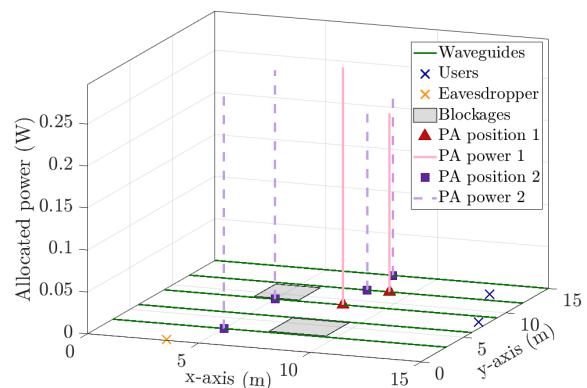
with $\kappa^2 = 0.1$. Simulation-specific parameters are detailed in the captions of the respective figures.

To begin with, we evaluate the effectiveness of the proposed geometry-aware upper bound on channel errors derived in (19), exploiting 10000 random channel realizations drawn from the prescribed uncertainty regions. We compare the following three quantities: (i) the actual channel error computed via Monte Carlo using (18), (ii) the conventional near-field linear error bound from [16], and (iii) the proposed upper bound obtained from (16). The performance metric is the normalized channel-error percentage, $\|\mathbf{H}_{E_g} - \hat{\mathbf{H}}_{E_g}\| / \|\hat{\mathbf{H}}_{E_g}\|$. Fig. 5 plots the normalized error versus orientation error and location error in subplots (a) and (b), respectively. Owing to the distributed PA locations, the existing linear bound [16], [23] is excessively loose. It is attributed that phase contributions from different PAs may partially cancel under small positional or angular perturbations, producing a sublinear growth of CSI error. Consequently, as the EA moves farther away and path phases become largely uncorrelated with the nominal geometry, the error saturates, yielding a flattening of the curve at large position errors. These behaviors demonstrate that the EA CSI mismatch is highly nonlinear, validating the need for the proposed geometry-aware uncertainty bound.

For comparison, we evaluate the proposed scheme in the presence and absence of blockages, labeled as “*Pro. w blk*” and “*Pro. w/o blk*”, respectively, against five benchmark schemes. Specifically, we consider: (i) “*Upper bound*”, which shares the same setting as the considered model except that both blockages and EAs are removed and the power attenuation along the waveguides is ignored, thus providing an optimistic performance upper bound; (ii) “*BM1 w blk*”, which adopts a fixed uniformed distributed beamforming strategy with half of the transmit power allocated to AN and the other half to the information signal, while the total power is equally distributed among all PAs, so that performance improvements only stem from optimizing the PA positions under realistic blockage conditions; (iii) “*BM1 w/o blk*”, which shares the same configuration as “*BM1 w blk*” but assumes an ideal environment without blockages; (iv) “*BM2 w blk*”, which employs a conventional BS precoder design while all PAs are fixed at their feed points and blockage effects are taken into



(a) Average achievable sum rate versus the total transmit power budget, P_{\max} , of different antenna configurations.



(b) Representative snapshot of the optimized PA locations and per-PA power allocations for $P_{\max} = 30$ dBm under blockage-aware and blockage-free designs.

Fig. 7. Average achievable sum rate versus the total transmit power budget of different antenna configurations under $N = 2$, $M = 5$, $G = 1$, $T = 2$ and $K = 2$, with a snapshot example of optimized PA locations and power allocations.

account; and (v) “*BM2 w/o blk*”, which is identical to “*BM2 w blk*” except that it assumes no blockages. For completeness, we also implement a “*Naive*” scheme that first optimizes the resource allocation while neglecting waveguide attenuation and blockage impacts, and then re-evaluates the resulting solution under the realistic attenuation and blockage conditions; if the obtained solution violates the power constraint (C3), we enforce $p_{n,m} = p_{n,m}^{\max}$, $\forall n, m$ as it is the maximum available power in that particular PA position and if it violates the information-leakage constraint (C6), the achievable sum rate is penalized to zero. Note that this naive scheme almost always yields zero performance due to simultaneous violations of the power and information-leakage constraints, its results are omitted from the plots.

We next examine the impact of the total power budget and the PA configuration, as illustrated in Fig. 7(a). As P_{\max} increases, all schemes exhibit a monotonic increase in the average sum rate, but with markedly different growth rates. The fixed-antenna baselines (BM2 with and without blockages) show only modest improvements, since their performance is fundamentally limited by the lack of spatial flexibility at the PA side. In contrast, both proposed designs, with and without

blockages, can more effectively exploit the additional transmit power, which leads to a significantly larger rate increase as P_{\max} grows. The upper-bound curve, obtained from an idealized system with no eavesdropper threat, waveguide attenuation, or blockage effects, achieves the highest rates. It can be observed that the sum rate gap between proposed schemes and the upper bound is slightly enlarged as P_{\max} increases. This is because, although a larger total power budget provides more available resources, the presence of an eavesdropper requires allocating a portion of the power to artificial noise rather than entirely devoting it to information beamforming. Notably, the gap between the two proposed curves (with and without blockages) remains relatively small over the entire considered power range. In contrast, the corresponding gap between the fixed-antenna baselines is much larger. This indicates that PA flexibility substantially mitigates the detrimental impact of blockages and enables the system to utilize the available transmit power budget into sum rate gains more efficiently. As the presence of blockages inevitably removes some PA-position candidates, the blockage-aware design still performs slightly below the ideal blockage-free case.

Fig. 7(b) illustrates a representative snapshot of the optimized PA deployment and power allocation for $P_{\max} = 30$ dBm, with two rectangular blockages whose lengths are 4.34 m and 3.19 m and whose heights are 7.75 m and 5.36 m, respectively. For clarity, only their ground projections are shown as grey rectangles. It can be noted that the active PAs are generally located near the centroid of the user cluster, balancing waveguide and wireless path losses. Specifically, among the 10 available PAs, the blockage aware design *Pro. w blk*, given by PA position 1 and PA power 1, activates two elements to serve the $K = 2$ users, whereas the design optimized for an ideal blockage-free environment, denoted by *Pro. w/o blk* with PA position 2 and PA power 2, activates four. Although the blockages constrain feasible PA locations for serving legitimate users, they can be exploited as physical shields that partially obstruct the LoS to EA, allowing the blockage-aware design to concentrate more transmit power on the information-carrying beams and rely less on AN generation.

Fig. 8 shows the average system sum rate versus the maximum normalized users' channel estimation error variance κ^2 for different configurations and EA uncertainty levels and for different EA-uncertainty and blockage configurations, comparing the proposed design with the two BM1 baselines. For all schemes, the average sum rate decreases as κ^2 increases, since a larger estimation error variance yields less accurate CSI at the BS. As a result, the information beamformer and AN precoder become more conservative in forming energy-focusing beams, and the optimized PA positions cannot ensure precise phase alignment with the legitimate users, thereby jointly reducing the received signal power and increasing residual interference. Despite this degradation, the proposed scheme consistently achieves a much higher sum rate than both BM1 baselines over the entire range of κ^2 and for all blockage configurations. This confirms that the joint optimization of BS beamforming and PA power-ratio and positions exploits the available spatial degrees of freedom for secure transmission

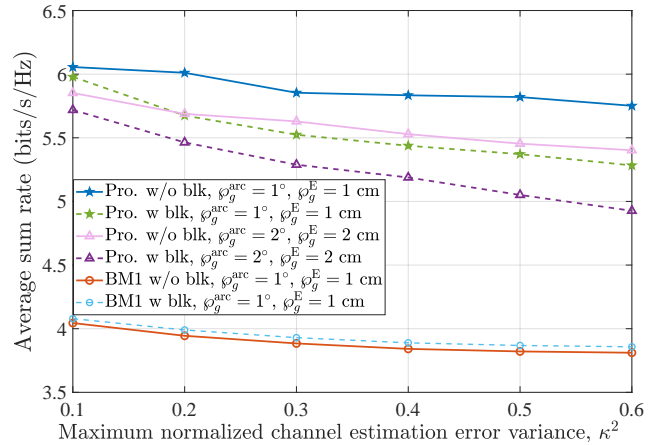


Fig. 8. Average sum rate versus the maximum normalized channel estimation error variance κ^2 with $K = 2$, $G = 1$, $T = 2$, $P_{\max} = 20$ dBm, and $R_{\text{tot}} = 1$ bits/s/Hz.

more efficiently, even under CSI and positioning uncertainties. Moreover, the rate gap between “*Pro. w blk*” and “*Pro. w/o blk*” widens as κ^2 grows, because inaccurate CSI limits the ability of the BS to compensate for blockage-induced power loss adaptively. In contrast, the curves for “*BM1 w blk*” and “*BM1 w/o blk*” almost overlap, since BM1 uses a fixed beamformer with uniform power allocation and thus depends only weakly on CSI; this makes BM1 less sensitive to CSI errors but also explains its significantly lower sum rate compared with the proposed joint design.

VII. CONCLUSION

In this paper, we proposed a blockage-aware PA-assisted multi-waveguide architecture for secure and robust down-link transmission under imperfect CSI. By developing a 3D blockage-aware channel model that jointly captures waveguide attenuation, free-space propagation, and geometry-based LoS conditions, together with a geometry-aware CSI uncertainty bound for distributed multi-antenna eavesdroppers, we formulated a robust sum-rate maximization problem that jointly optimizes beamforming, AN covariance, PA power-ratio allocation, and PA positions under secrecy constraints. The resulting highly non-convex design was tackled via a BCD-based algorithm leveraging S-procedure and MM-based reformulations, including a physically motivated two-stage PA positioning strategy that separates large-scale movement in regard to path loss and blockage-aware channel coefficients impacts and small-scale adjustment with respect to phase shift alignments. Simulation results verified the tightness of the proposed channel uncertainty model and demonstrated substantial performance gains compared with conventional fixed-antenna baselines. These findings highlight the value of incorporating spatial blockages into secure communication design, especially revealing that ignoring blockage can cause severe performance degradation and even infeasible secrecy constraints. In contrast, adaptive PA positioning can preserve LoS for legitimate users, disrupt eavesdroppers' channels, and reduce the AN power required to meet secrecy targets.

REFERENCES

- [1] R. Zhao, S. Hu, D. Mishra, and D. W. K. Ng, "Resource allocation for multi-waveguide pinching antenna-assisted broadcast networks," *arXiv preprint arXiv:2507.03915*, 2025.
- [2] Y. Wu, D. Xu, D. W. K. Ng, W. Gerstacker, and R. Schober, "Movable antenna-enhanced multiuser communication: Jointly optimal discrete antenna positioning and beamforming," in *Proc. IEEE Global Telecommun. Conf.*, Dec. 2023, pp. 7508–7513.
- [3] K.-K. Wong, A. Shojaefard, K.-F. Tong, and Y. Zhang, "Fluid antenna systems," *IEEE Trans. Wirelss Commun.*, vol. 20, no. 3, pp. 1950–1962, Mar. 2021.
- [4] Z. Ding, R. Schober, and H. V. Poor, "Flexible-antenna systems: A pinching-antenna perspective," *IEEE Trans. Commun.*, vol. 73, no. 10, pp. 9236–9253, Oct. 2025.
- [5] X. Xu, X. Mu, Z. Wang, Y. Liu, and A. Nallanathan, "Pinching-antenna systems (PASS): Power radiation model and optimal beamforming design," *arXiv preprint arXiv:2505.00218*, 2025.
- [6] Z. Wang, C. Ouyang, X. Mu, Y. Liu, and Z. Ding, "Modeling and beamforming optimization for pinching-antenna systems," *IEEE Trans. Commun.*, early access, Oct. 13, 2025, doi: 10.1109/TCOMM.2025.3621049.
- [7] H. Li, Z. Lyu, Y. Gao, M. Xiao, and H. V. Poor, "MIMO pinching-antenna-aided SWIPT," *IEEE Wireless Commun. Lett.*, early access, Oct. 08, 2025, doi: 10.1109/LWC.2025.3618988.
- [8] S. A. Tegos, P. D. Diamantoulakis, Z. Ding, and G. K. Karagiannidis, "Minimum data rate maximization for uplink pinching-antenna systems," *IEEE Wireless Commun. Lett.*, vol. 14, no. 5, pp. 1516–1520, May 2025.
- [9] Y. Xu, D. Xu, X. Yu, S. Song, Z. Ding, and R. Schober, "Joint radiation power, antenna position, and beamforming optimization for pinching-antenna systems with motion power consumption," *arXiv preprint arXiv:2507.02348*, 2025.
- [10] K. Guo, C. Wang, Z. Li, D. W. K. Ng, and K.-K. Wong, "Multiple UAV-borne IRS-aided millimeter wave multicast communications: A joint optimization framework," *IEEE Commun. Lett.*, vol. 25, no. 11, pp. 3674–3678, Nov. 2021.
- [11] P. Yi, L. Zhu, Z. Xiao, R. Zhang, Z. Han, and X.-G. Xia, "Trajectory design and resource allocation for multi-UAV communications under blockage-aware channel model," *IEEE Trans. Commun.*, vol. 72, no. 4, pp. 2324–2338, Apr. 2024.
- [12] Z. Ding and H. V. Poor, "LoS blockage in pinching-antenna systems: Curse or blessing?" *IEEE Wireless Commun. Lett.*, vol. 14, no. 9, pp. 2798–2802, Sep. 2025.
- [13] K. Wang, C. Ouyang, Y. Liu, and Z. Ding, "Pinching-antenna systems with LoS blockages," *IEEE Wireless Commun. Lett.*, early access, Sep. 24, 2025, doi: 10.1109/LWC.2025.3614451.
- [14] P. Yi, L. Zhu, L. Zhu, Z. Xiao, Z. Han, and X.-G. Xia, "Joint 3D positioning and power allocation for UAV relay aided by geographic information," *IEEE Trans. Wireless Commun.*, vol. 21, no. 10, pp. 8148–8162, Oct. 2022.
- [15] X. Yu, D. Xu, Y. Sun, D. W. K. Ng, and R. Schober, "Robust and secure wireless communications via intelligent reflecting surfaces," *IEEE J. Sel. Areas Commun.*, vol. 38, no. 11, pp. 2637–2652, Nov. 2020.
- [16] Z. Ren, S. Zhang, L. Qiu, D. W. K. Ng, and J. Xu, "Robust secure communications in near-field ISCAP systems with extremely large-scale antenna array," *arXiv preprint arXiv:2505.15279*, 2025.
- [17] K. Wang, Y. Liu, and Z. Ding, "Pinching-antenna systems for physical layer security," *IEEE Wireless Commun. Lett.*, early access, Oct. 23, 2025, doi: 10.1109/LWC.2025.3624885.
- [18] M. Sun, C. Ouyang, S. Wu, and Y. Liu, "Physical layer security for pinching-antenna systems (PASS)," *arXiv preprint arXiv:2503.09075*, 2025.
- [19] O. S. Badarneh, H. S. Silva, and Y. H. A. Badarneh, "Physical-layer security of pinching-antenna systems," *arXiv preprint arXiv:2503.18322*, 2025.
- [20] N. Su, F. Liu, and C. Masouros, "Sensing-assisted eavesdropper estimation: An ISAC breakthrough in physical layer security," *IEEE Trans. Wireless Commun.*, vol. 23, no. 4, pp. 3162–3174, Apr. 2024.
- [21] G. Zhou, V. Papanikolaou, Z. Ding, and R. Schober, "Channel estimation for mmWave pinching-antenna systems," in *Proc. IEEE 26th Int. Workshop Signal Process. Adv. Wireless Commun. (SPAWC)*, Jul. 2025, pp. 1–5.
- [22] J. Yao, J. Xu, W. Xu, D. W. K. Ng, C. Yuen, and X. You, "Robust beamforming design for RIS-aided cell-free systems with CSI uncertainties and capacity-limited backhaul," *IEEE Trans. Wireless Commun.*, vol. 71, no. 8, pp. 4636–4649, Aug. 2023.
- [23] Y. Xiu, Y. Zhao, S. Yang, Y. Zhang, D. Niyato, H. Du, and N. Wei, "Robust beamforming design for near-field DMA-NOMA mmwave communications with imperfect position information," *IEEE Trans. Wireless Commun.*, vol. 24, no. 2, pp. 1678–1692, Feb. 2025.
- [24] S. Hu, Z. Wei, Y. Cai, C. Liu, D. W. K. Ng, and J. Yuan, "Robust and secure sum-rate maximization for multiuser MISO downlink systems with self-sustainable IRS," *IEEE Trans. Commun.*, vol. 69, no. 10, pp. 7032–7049, Oct. 2021.
- [25] M. Zeng, X. Wang, Y. Liu, Z. Ding, G. K. Karagiannidis, and H. V. Poor, "Robust resource allocation for pinching-antenna systems under imperfect CSI," *arXiv preprint arXiv:2507.12582*, 2025.
- [26] S. Hu, R. Zhao, Y. Liao, D. W. K. Ng, and J. Yuan, "Sum-rate maximization for pinching antenna-assisted NOMA systems with multiple dielectric waveguides," *arXiv preprint arXiv:2503.10060*, 2025.
- [27] C. A. Balanis, *Balanis' Advanced Engineering Electromagnetics*. John Wiley & Sons, 2024.
- [28] R. J. Mailloux, *Phased array antenna handbook*. Artech house, 2017.
- [29] M. Cui and L. Dai, "Channel estimation for extremely large-scale MIMO: Far-field or near-field?" *IEEE Trans. Commun.*, vol. 70, no. 4, pp. 2663–2677, Apr. 2022.
- [30] Y. Liu, Z. Wang, X. Mu, C. Ouyang, X. Xu, and Z. Ding, "Pinching-antenna systems: Architecture designs, opportunities, and outlook," *IEEE Commun. Mag.*, early access, Sep. 17, 2025, doi: 10.1109/MCOM.001.2500037.
- [31] A. Berehlyk, C. Ouyang, S. Asaad, Z. Ding, and H. V. Poor, "MIMO-PASS: Uplink and downlink transmission via MIMO pinching-antenna systems," *arXiv preprint arXiv:2503.03117*, 2025.
- [32] S. Sun, T. S. Rappaport, T. A. Thomas, A. Ghosh, H. C. Nguyen, I. Z. Kovacs, I. Rodriguez, O. Koymen, and A. Partyka, "Investigation of prediction accuracy, sensitivity, and parameter stability of large-scale propagation path loss models for 5G wireless communications," *IEEE Trans. Veh. Technol.*, vol. 65, no. 5, pp. 2843–2860, May 2016.
- [33] Z. Chen, F. Wang, G. Han, X. Wang, and V. K. Lau, "Robust beamforming design for secure near-field ISAC systems," *IEEE Wireless Commun. Lett.*, vol. 14, no. 10, pp. 3089–3093, Oct. 2025.
- [34] Z. Xing, R. Wang, X. Yuan, and J. Wu, "Location information assisted beamforming design for reconfigurable intelligent surface aided communication systems," *IEEE Trans. Wireless Commun.*, vol. 22, no. 11, pp. 7676–7695, Nov. 2023.
- [35] Y. Xu, Z. Ding, and G. K. Karagiannidis, "Rate maximization for downlink pinching-antenna systems," *IEEE Wireless Commun. Lett.*, vol. 14, no. 5, pp. 1431–1435, May 2025.
- [36] H. O. Y. Suzuki and K. Kawai, "Pinching antenna: Using a dielectric waveguide as an antenna," *NTT DOCOMO Technical J*, 2022.
- [37] P. Ramezani, Ö. Tuğfe Demir, and E. Björnson, "Localization in massive MIMO networks: From Far-Field to Near-Field," *Massive MIMO for Future Wireless Communication Systems: Technology and Applications*, pp. 123–150, 2025.
- [38] M. Zhang, X. Yuan, B. Teng, and L. Wang, "Array partitioning based near-field attitude and location estimation," in *Proc. 16th Int. Conf. Wireless Commun. Signal Process. (WCSP)*, Oct. 2024, pp. 813–818.
- [39] J. Cheng, K. Guan, and F. Quirin, "Direction-of-arrival estimation with virtual antenna array: Observability analysis, local oscillator frequency offset compensation, and experimental results," *IEEE Trans. Instrum. Meas.*, vol. 70, pp. 1–13, Jun. 2021.
- [40] R. Schmidt, "Multiple emitter location and signal parameter estimation," *IEEE Trans. Antennas Propag.*, vol. 34, no. 3, pp. 276–280, Mar. 1986.
- [41] K. Okamoto, *Fundamentals of optical waveguides*. Elsevier, 2021.
- [42] D. W. K. Ng, S. Leng, and R. Schober, "Multiple antennas and beamforming for SWIPT systems." 2016.
- [43] G. Zhu, X. Mu, L. Guo, S. Xu, Y. Liu, and N. Al-Dhahir, "Pinching-antenna systems (PASS)-enabled secure wireless communications," *arXiv preprint arXiv:2504.13670*, 2025.
- [44] Y. Wu, D. Xu, D. W. K. Ng, W. Gerstacker, and R. Schober, "Globally optimal movable antenna-enabled multiuser communication: Discrete antenna positioning, power consumption, and imperfect CSI," *IEEE Trans. Commun.*, vol. 73, no. 10, pp. 9903–9923, Oct. 2025.
- [45] Z. Mao, W. Wang, Q. Xia, C. Huang, X. Pan, and Z. Ye, "Amplitude-dependent phase-gradient directional beamforming for IRS: A scalable optimization framework," *IEEE Trans. Wirelss Commun.*, vol. 72, no. 4, pp. 2354–2369, Apr. 2024.
- [46] X. Yu, D. Xu, D. W. K. Ng, and R. Schober, "IRS-assisted green communication systems: Provable convergence and robust optimization," *IEEE Trans. Commun.*, vol. 69, no. 9, pp. 6313–6329, Sep. 2021.
- [47] J. Mairal, "Incremental majorization-minimization optimization with application to large-scale machine learning," *SIAM J. Optim.*, vol. 25, no. 2, pp. 829–855, 2015.